

A Cost Effective Approach for Subsonic Aeroelastic Stability Analysis of Turbomachinery 3D Blade Cascade. A Reduced Order Aeroelastic Model Numerical Approach

Chandra Shekhar Prasad (✉ cprasad@it.cas.cz)

Institute of Thermomechanics Czech Academy of Sciences: Ustav termomechaniky Akademie ved Ceske republiky <https://orcid.org/0000-0002-3087-5807>

Radek Kolman

Institute of Thermomechanics Czech Academy of Sciences: Ustav termomechaniky Akademie ved Ceske republiky

Ludek Pesek

Institute of Thermomechanics Czech Academy of Sciences: Ustav termomechaniky Akademie ved Ceske republiky

Research Article

Keywords: Aeroelastic-instability, classical-flutter, Unsteady panel method (UPM), reduced order aeroelastic model (ROAM), boundary element method (BEM), 3D blade cascade

Posted Date: March 10th, 2021

DOI: <https://doi.org/10.21203/rs.3.rs-252660/v1>

License: © ⓘ This work is licensed under a Creative Commons Attribution 4.0 International License.

[Read Full License](#)

A cost effective approach for subsonic aeroelastic stability analysis of turbomachinery 3D blade cascade

A reduced order aeroelastic model numerical approach

Chandra Shekhar Prasad · Radek Kolman · Luděk Pešek

Received: date / Accepted: date

Abstract In this paper a cost effective numerical model for subsonic classical flutter analysis for turbomachinery is presented. The model is based on reduced order aeroelastic modeling (ROAM) approach. The prime objective of the ROAM is to significantly reduce the computational time for flutter analysis of low pressure (LP) stage blades of power turbines at preliminary design stage. A mesh free incompressible fluid solver based on boundary element method (BEM) e.g. 3D panel method is developed. The proposed ROAM is employed to perform subsonic aeroelastic stability analysis in 3D blade cascades. The ROAM simulated results are compared against experimental and high fidelity CFD-CSD model's results. The ROAM estimated results show good agreement with experimental results and prove to be much faster in execution compared to CFD-CSD model. Therefore, this gives designers and engineers a freedom to analyze multiple design iteration in very short time on normal workstation. Thus, the ROAM has immense potential for industrial use as a cost effective and faster numerical tool for design and analysis of more efficient and safer power turbines to meet the future demand of electric energy cheaply, quickly and efficiently.

Keywords: Aeroelastic-instability, classical-flutter, Unsteady panel method (UPM), reduced order aeroelastic model (ROAM), boundary element method (BEM), 3D blade cascade.

1 Introduction:

The power turbines are undoubtedly plays a crucial role in electricity generation cycle in majority of the present day's power plants if we exclude the renewable energy power generation plants. Their designer have face challenging task to insure the safety and reliability of large power turbine for uninterrupted electrical power supply. More advance and larger power turbines are being manufactured to harness maximum energy from steam volume to meet the increasing energy demand. One of the example of such large steam turbine is Arabelle turbines which has low pressure (LP) stage blade length reaches up to 1.9 m. According to it's manufacturer GE power of United State, currently Arabelle turbines are used by one-third of world's nuclear power plants [1]. Since these machine operates in a very harsh flow environment and subjected to enormous mechanical stresses which can lead to catastrophic failure. Specifically the LP stage blade assemblies

Flutter or flow induced vibration, perhaps is one of the most catastrophic among all of them [2]. Flutter is an aeroelastic instability phenomena frequently occurs in turbomachinery devices, and thus, remains a major design challenge in turbomachinery design process. The long thin blades of LP stage are more susceptible to flow induced vibrations or flutter due to low material shiftiness [3]. This leads to pre-mature structural failure and demands frequent maintenance which can be costly.

Institute of Thermomechanics
Prague, Czech Republic
Tel.: +420-26-6053018
Fax: +420-28-6584695
E-mail: cprasad@it.cas.cz

Institute of Thermomechanics
Prague, Czech Republic
E-mail: kolman@it.cas.cz

Institute of Thermomechanics
Prague, Czech Republic
E-mail: pesek@it.cas.cz

In principle a flutter phenomena in power turbine blades is consequence of the phase lag between excitation (fluid force exerted on the structure) and response of the structure. However, the phase lag not always amplifies the vibration and leads to flutter or aeroelastic instability, in opposite in some situations, this phase lag damps the vibration. Therefore, all the possible reason for such behaviors are still unknown and mostly under investigations. Moreover, in the past researches it is observed that even if a oscillating structure absorbs energy from surrounding fluid the oscillation would not amplify to flutter, if there is sufficient structural damping present to overcome the excitation force [4]. Therefore, it somehow proves that the flutter strongly linked to the flexibility of the structure. The Fig.1 shows different type of flutter which commonly occurs in turbomachines. In this flutter chart a,b and c type of flutter is more likely to occur in steam turbine whereas,d,e and f more common in gas turbines. This research is focused

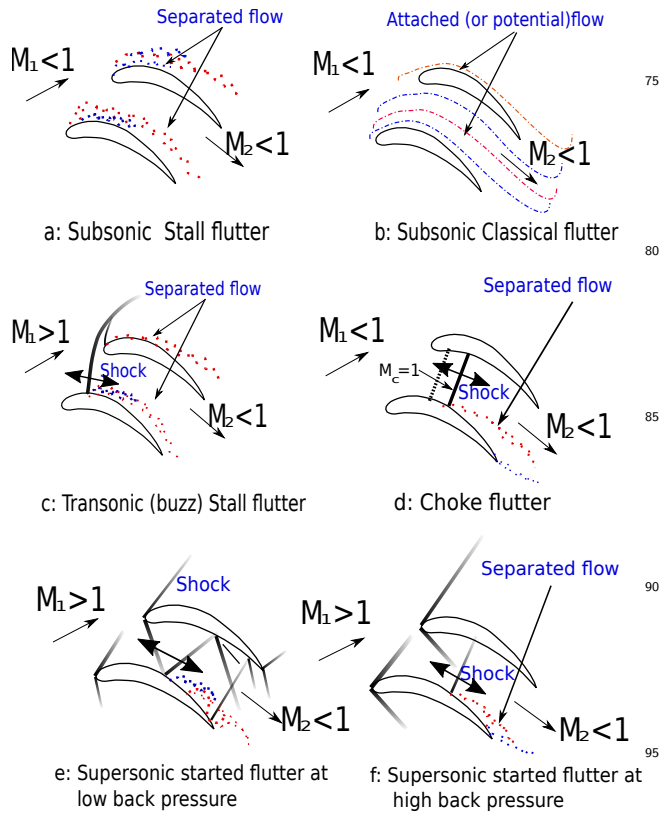


Fig. 1 Flutter chart for in the turbomachinery

on subsonic flutter at low amplitude and low frequency in attached flow which often termed as Classical (or potential flow) flutter which corresponds to Fig.1 (b). Classical flutter is one of the dominating aeroelastic stability problem, and needs careful attention in the pre-

liminary design stage. Another justification to study the classical flutter is that if the blade assembly is aeroelastically unstable for lower and less chaotic flow field, then it is highly likely for non-linear flow regime system will be much more unstable [5]. Therefore, the study of aeroelastic stability in power turbine remains an active research topic for researchers and engineers in past and recent years [6, 7].

Aerodynamic damping (AD)/work is used as key parameter for aeroelastic stability analysis turbomachinery blade cascade [5, 8, 9]. A large numbers of design iterations are required to optimize the blade geometry and the arrangement of blade cascade for aeroelastic stability in short period of time. In the preliminary design stage the numerical tools are preferred for design iteration to save both time and cost. Currently fully or loosely coupled high fidelity CFD-CSD based numerical tools are used by industry and researcher. Though they yield quite accurate results, these tools are computationally very expensive and demands large supercomputers to execute. Furthermore, it is often in the CFD-CSD type of tools fluid solver part (CFD) is accounted for the majority of computation time.

Objective: Therefore, this research work is profoundly motivated by the fact to come up with an alternative cost effective reduced order aeroelastic numerical model(ROAM) which can be good compromise of speed and accuracy to analyze the aerodynamic stability issue in power turbine. Novelty of the paper lies in the use of medium fidelity BEM 3D PM for stability analysis of 3D blade cascade including the tunnel wall effect. To the best of authors knowledge this has not been attempted in the past.

The boundary element method e.g. 3D surface panel method(PM) is one of such methods for fluid flow modeling. It was first proposed by Hess and Smith [10] to model the lifting and non-lifting potential flow around slender bodies. These methods are a good compromise of speed and accuracy and can be used for complex geometry until the flow field fulfills the criteria of potential flow without separation which is the case of classical flutter. However, modified PM can be used for the separated flow case [11]. These methods are comprehensively adopted for aerodynamics/aeroelastic modeling of wind turbines [12, 13, 14], helicopter rotors [15, 16], ship propeller[17] and aircraft aeroelasticity [18]. A ROM approach for wind turbine aeroelasticity is adopted by Rezaei et al.[19] More details about theoretical and numerical implementation of PM can be found in Katz [20].

However, instead of immense potential of the PM to be used in LP turbine aeroelasticity very few researcher have pondered it in this field. An improved version

of PM is used by [21, 22] for 2D cascade design and flow modeling, in his work only pressure distribution is estimated, whereas [23] used the similar technique to estimate the aeroelastic stability parameters, but in this work only camber surface of the blade is modeled not the actual geometry. Furthermore, Ramierez et al. [24] employed a modified version of PM with viscous-inviscid coupling technique to study the boundary layer separation and the aerodynamic characteristics in the rectilinear 2D blade cascade. In an other study Chen et al. [25] have used a 2D frequency domain source-doublet based PM to estimate the 2D and quasi 3D blade loading in centrifugal type turbomachinery system. But as we discussed earlier majority the previous work involving PM for turbomachinery cascade flow are limited to merely 2D and steady flow analysis cases according to best of author's knowledge.

Though PM is not favored by researcher in the past in aeroelastic stability problem for turbomachinery, but PM remains on of the preferred choice for inverse optimization tool for turbomachinery blade cascade due to its capability to handle complex geometry and fast execution time compared to field element based methods (CFD). Since inverse optimization requires multiple iteration for small design change, there is not doubt why researchers in this field have favored BEM-PM or similar method. Some of the recent and more significant examples of use of PM for inverse optimization problem of axial compressor and turbine blade cascade optimization are [26, 27, 28, 29]. Moreover, less sophisticated 3D unsteady vortex lattice method (UVLM) type boundary element method were used by [30, 31, 32]. More details about advantages of PM over UVLM can be found in Katz [20],[11].

Majority of the time PM is used for the external aerodynamics modeling, also in the above mentioned applications for power turbine cases external PM method is adopted. The presence of wind tunnel walls around a test model significantly changes the flow field around the test subject due to blockage effect [33]. Therefore, it is very crucial to include the wall effects in the numerical model too. Thus, in the present research wind tunnel effect is considered and modeled using constant source elements. In past researchers have successfully managed wind tunnel wall effects to test subject. The PM is used by Wang et al. [34] to include tunnel wall effect on model wind turbine, Ashby et al. [35] used PM based solver VSAERO for modeling of turning vanes in tunnel, Demiroglu et al.[33] in their work they have studied the both 2D and 3D configuration of tunnel wall effects using PM.

Furthermore, to estimate the aerodynamic damping most common methods are traveling wave mode

(TWM) method and less known aerodynamic influence coefficient (AIC) method [5, 36]. For the present research work TWM method is adopted because it is more representative to actual vibration pattern in the power turbine rotor. A detail explanation of both the methods can be found in Fransson [5]. The estimation of AD in TWM using panel method in 2D case is also adopted by [37]. In the sub Fig.2(a) and (b) a 3D representation of

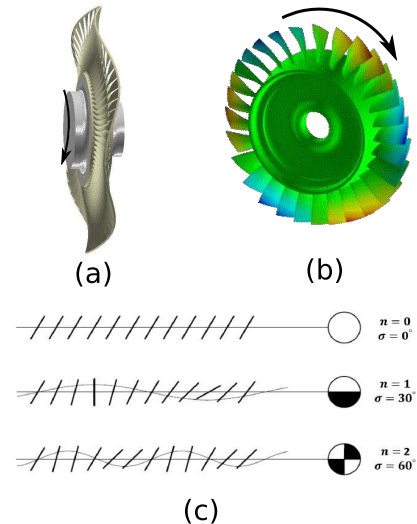


Fig. 2 TWM oscillation and IBPA: (a) and (b) 3D representation of TW with 5 and 3 ND [38, 39] (c) 2D representation of TWM (ND=12);torsional flutter in linear cascade [40]

the TW is shown and the in the sub Fig.2 (c) a 2D TW presented. A good details about TWM is presented by According to Crawley [41]. An other important parameter in the turbomachinery blade flutter study is reduced frequency (k). It was first highlighted by Maldahl [42], and can be expressed by Eq. 1

$$k = \frac{2\pi f c}{V} \quad (1)$$

where f is the oscillation frequency(Hz), c the blade chord and V the flow velocity. For the classical flutter k value should be $k < 0.3$.

2 Unsteady 3D surface Panel method for flow modeling

3D Surface panel methods can be employed for aerodynamic model lifting and non-lifting surfaces using the potential flow assumptions. The flow field is inviscid ($\text{Viscosity } (\eta) = 0$) and rotational ($\nabla \times \mathbf{V} = 0$). The rectangular singularity panel elements are placed on the

entire solid surface and in the wake, these singularity elements are the known solutions to Laplace's Eq. (2).

$$\nabla^2 \Phi(x, y, z) = \frac{\partial^2 \Phi}{\partial^2 x} + \frac{\partial^2 \Phi}{\partial^2 y} + \frac{\partial^2 \Phi}{\partial^2 z} = 0 \quad (2)$$

where $\Phi(x, y, z)$ is the scalar velocity potential and it is function of (x, y, z) such that $(V = \nabla \Phi)$. Apart from singularity distributions appropriate boundary conditions are required to find the unique solution of Laplace's Eq. (2). The required BCs are, (1) enforcing the impermeability flow at solid or a fixed normal flow condition ($\nabla \Phi \cdot \mathbf{n} = V_n = 0$), (2) Far field: The disturbance created by the singularities on the body and wake must disappear at infinity ($\lim_{|r| \rightarrow \infty} \nabla(\Phi - \Phi_\infty) = 0$). (3) the Kutta condition and Kelvin's theorem, are imposed in order to obtain a complete description of the flow field and the resulting aerodynamic loads. The pressure field (p) is then by obtained solving the unsteady Bernoulli's equation.

Fig.3 plots a cross-section of the wing and flow field,

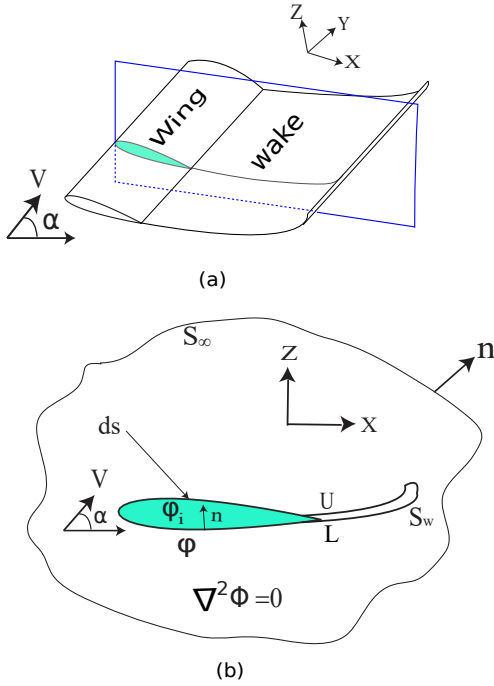


Fig. 3 Cross section of wing with time dependent wake panels

demonstrating that there are two flow regions, the external flow around the wing and the internal flow inside¹⁷⁵ the wing. The potential functions Φ and Φ_i are the external and internal velocity potentials of the flow field. Panel methods solve Laplace's equation using Green's identity for the volume enclosed by the two regions. The total potential induced at any point P (external of¹⁸⁰

internal) is given by

$$\begin{aligned} \Phi(P) = & \frac{1}{4\pi} \iint_{S_B} \mu_b \mathbf{n} \cdot \nabla \left(\frac{1}{r} \right) ds \\ & - \frac{1}{4\pi} \iint_{S_B} \sigma_b \left(\frac{1}{r} \right) ds \\ & + \frac{1}{4\pi} \iint_{S_w} \mu_w \mathbf{n} \cdot \nabla \left(\frac{1}{r} \right) ds + \Phi_\infty \end{aligned} \quad (3)$$

where Φ_∞ is the potential induced by the free stream, σ_b and μ_b are source and doublet strength distributions over the body respectively, μ_w is the doublet strength distribution over the wake, S_B is the surface area of the body and S_w is the surface area of the wake. The doublet and source strengths in Eq. (3) are defined as

$$-\mu = \Phi - \Phi_i \quad (4)$$

$$-\sigma = \frac{\partial \Phi}{\partial n} - \frac{\partial \Phi_i}{\partial n} = \nabla(\Phi - \Phi_i) \cdot \mathbf{n} \quad (5)$$

The Eq. (3) can be employed to estimate the induced potential at any arbitrary point with proper BC. Here it is achieved by imposing internal Dirichlet along with three earlier mentioned BC. Thus, with suitable BC's Eq. (3) can be reduced to an algebraic form once it is solved for all collocation points and can be given by Eq. (6)

$$\sum_{k=1}^{N_B} \mu_{b_k} A_{j,k} + \sum_{k=1}^{N_B} \sigma_{b_k} B_{j,k} + \sum_{k=1}^{N_W} \mu_{w_k} C_{j,k} = 0 \quad (6)$$

All three influence coefficient matrix can be given as

$$\begin{aligned} \mathbf{A}_{(N_b \times N_b)} &= \begin{pmatrix} a_{1,1} & a_{1,2} & \cdots & a_{1,N_b} \\ a_{2,1} & a_{2,2} & \cdots & a_{2,N_b} \\ \vdots & \vdots & \ddots & \vdots \\ a_{N_b,1} & a_{N_b,2} & \cdots & a_{N_b,N_b} \end{pmatrix} \\ \mathbf{B}_{(N_b \times N_b)} &= \begin{pmatrix} b_{1,1} & b_{1,2} & \cdots & b_{1,N_b} \\ b_{2,1} & b_{2,2} & \cdots & b_{2,N_b} \\ \vdots & \vdots & \ddots & \vdots \\ b_{N_b,1} & b_{N_b,2} & \cdots & b_{N_b,N_b} \end{pmatrix} \\ \mathbf{C}_{(N_b \times N_w)} &= \begin{pmatrix} c_{1,1} & c_{1,2} & \cdots & c_{1,N_w} \\ c_{2,1} & c_{2,2} & \cdots & c_{2,N_w} \\ \vdots & \vdots & \ddots & \vdots \\ c_{N_b,1} & c_{N_b,2} & \cdots & c_{N_b,N_w} \end{pmatrix} \end{aligned} \quad (7)$$

$\boldsymbol{\mu}_b = [\mu_{b_1} \dots \mu_{b_{N_b}}]^T$ is the vector of the unknown doublet strengths of the body surface panels, $\boldsymbol{\sigma}_b = [\sigma_1 \dots \sigma_{N_b}]^T$ is the vector of the unknown source strengths of the body surface panels, $\boldsymbol{\mu}_w = [\mu_{w_1} \dots \mu_{w_{N_w}}]^T$ is the vector of the unknown doublet strengths of the wake panels. N_B

is the number of body panels, N_W is the number of wake panels. Each elements of influence coefficient matrices \mathbf{A} i.e. $a_{i,j}$ represents the induced potential on i^{th} collocation point by j^{th} constant strength body doublet panel, similarly element of matrices \mathbf{B} i.e. $b_{i,j}$ represents the induced potential on i^{th} collocation point by j^{th} constant strength body source panel and element of matrices \mathbf{C} i.e. $c_{i,j}$ represents the induced potential on i^{th} collocation point by j^{th} wake doublet panel. The solution of Eq. (6) gives the value of unknown value of μ_k . The detailed description of solution method is well presented by [20].

Once the perturbation potential or unknown μ_b is known, the unsteady pressure coefficient can be calculated using instantaneous Bernoulli's equation and given as

$$\tilde{C}_p(x, y, t) = 1 - \frac{V_{total}^2}{V_\infty^2} - \frac{2}{V_\infty^2} \frac{\partial \mu}{\partial t} \quad (7)$$

where

$$V_{total} = V_{kinematic} + v_{perturbation}$$

In order to solve Eq. (7) in time domain, a time discretization method is needed. An implicit method is required, as the objective is to obtain the pressure coefficient at time $t + \Delta t$. Several methods to solved it , in the present case Backward Euler Method, which applied to Eq. (7) yields

$$\tilde{C}_p^{t+\Delta t} = 1 - \left(\frac{V_{total}^{t+\Delta t}}{V_\infty} \right)^2 - \frac{2}{V_\infty^2} \left(\frac{\mu^{t+\Delta t} - \mu^t}{\Delta t} \right) \quad (8)$$

More detailed discussion on numerical implementation and estimation of the aerodynamic loads can be found in [20]. Also the analytically solution for the 3D constant strength source (σ) and doublet (μ) singularity element is given in [20].

2.1 Panel method for the internal flow and tunnel wall effect simulation

There are two way to model the wall effect in the wall bounded internal aerodynamic using PM. 1) mirror image wall method, Fig.5(a) 2) direct wall method, Fig.5(b). A good review about both the methods can be found in the [43]. In this research direct wall method is adopted.

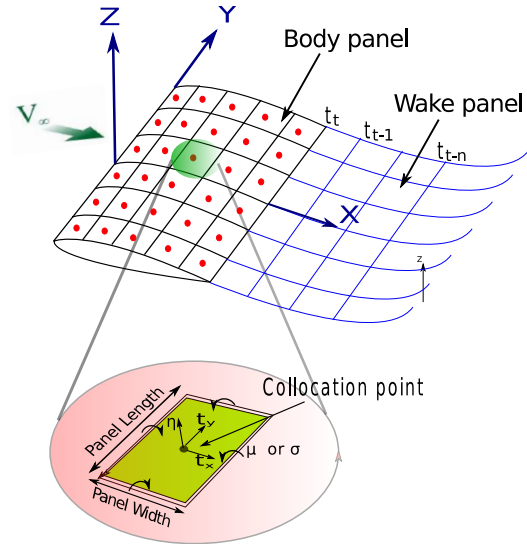


Fig. 4 PM discretization of wing using source and doublet singularities elements

2.1.1 Tunnel wall effect using direct wall method PM

The schematic diagram of 2D and 3D version of direct wall method is presented in Fig.6(a) and Fig.6(b) respectively. In order to simulated the wind tunnel wall effect on the flow field around the test object using PM, the wind tunnel walls are discretized into a numbers of panels, on which singularities can be distributed. Since the wind tunnel wall are no-lifting body, the constant strength source singularity elements can be used along with impermeability boundary condition (BC). The impermeability BC though tunnel wall can be achieved by zero normal flow ($V_n = \nabla \Phi \cdot \mathbf{n} = 0$) at the tunnel wall as shown in the Fig.6(a). The same BC is also true for the test object's solid surface as well. According to the Fig.6(a) velocity potential $\phi(P)$ at any arbitrary point P in the flow field, can the be the contribution of the free stream potential Φ_∞ and all the solid surface's (NS) singularity elements including wind tunnel walls and the wake panels (NS_w). Therefore, total potential at point P can be given by

$$\phi(P) = \Phi_\infty + \sum_{k=1}^{k=NS+NS_w} \Phi_{i_k} \quad (9)$$

In the present research this is accomplished by modeling the internal flow geometry as a closed box with the panel normal vectors pointing into the interior of the box Fig.6(b). Inflow and outflow of the box (flow through a tunnel) may be prescribed as normal velocities on groups of panels at the inlet and outlet face of the box. The inflow and outflow must be prescribed so that the continuity equation is satisfied. It should be noted here that, for the clarity of the visualization

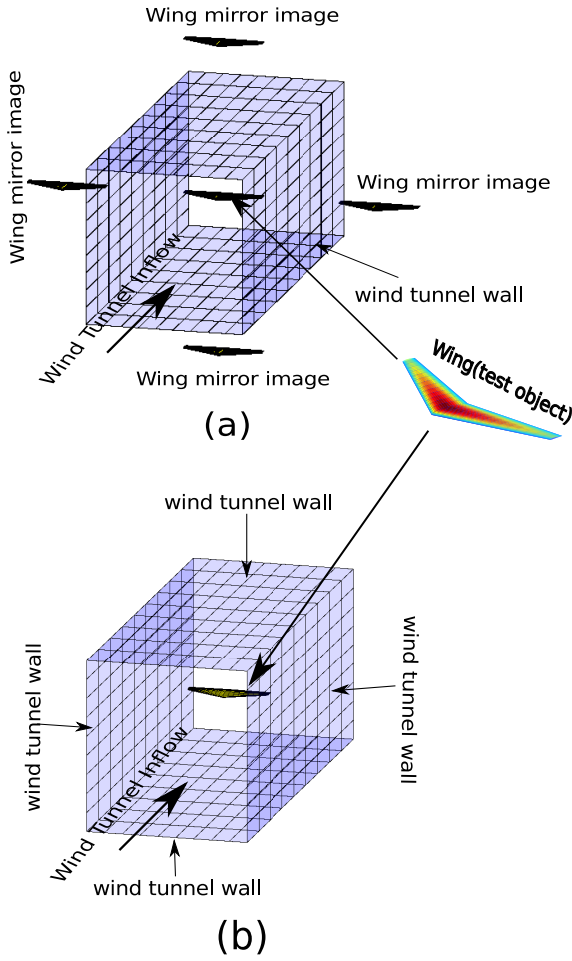


Fig. 5 Different method to simulate wall effects using PM (a) mirror image method (b) direct wall (source elements)method.

215 the inlet and out face grid panel are not displayed in the Fig.6(b), however it is taken into account in actual model. All the tunnel wall is discretized into rectangular panels and constant strength source (σ) singularity elements are distributed on it as shown in the Fig.6(b).

Furthermore, due to presence of wing doublet and source elements and wake doublet, the actual strength of the wall source strength will also be effected. Therefore, the actual source strengths (σ_w) on the wind tunnel wall can be calculated by imposing the Neumann BC of zero normal flow at the wall boundaries, and thus can be given by Eq. (10)

$$\sum_{i=1}^{i=N} D_{k,i} \mu_{b_i} + \sum_{i=1}^{i=N} G_{k,i} \sigma_{b_i} + \sum_{i=1}^{i=N_w} W_{k,i} \mu_{w_i} + \sum_{i=1}^{i=M} F_{k,i} \sigma_{w_i} = 0 \quad (10)$$

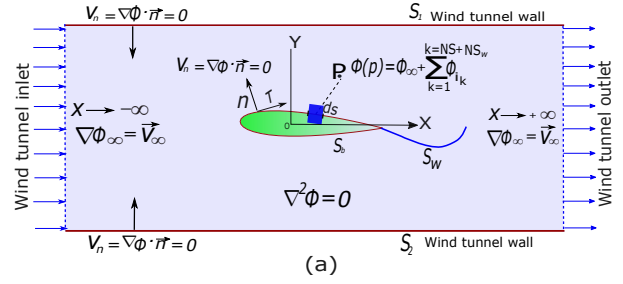


Fig. 6 Direct wall method to simulate wall effect in internal flow PM application .

220 where N is number of source and doublet panels on the wing surface, N_w number of wake panels and $K=1, M$ numbers of wind tunnel wall panels. And the influence coefficient matrix $D_{k,i}$, $G_{k,i}$, $W_{k,i}$ and $F_{k,i}$ are the normal components of velocity induced by the i th wing doublet, source, wake doublet and wall source panel on the k th wall panel. Since the μ_w , σ_b , and μ_w is known, this unknown value of wall source strength σ_w can be estimated by solving the Eq. (10) with Gaussian elimination method. A flowchart algorithm to estimate the wind tunnel wall effect using PM is presented in the Fig.7. The same strategy will be adopted here to simulate and model the unsteady aerodynamic flow around 3D blade cascade inside the wind tunnel section.

3 Classical flutter phenomena in turbomachinery blade cascade

225 In general if any mechanical structure or more specifically turbine blade is oscillating inside a fluid medium, then, either it supplies energy into surrounding fluid medium or absorbs energy from it or remains neutral during the specific vibration cycle. Furthermore, to describe it more clearly the former two phenomena is schematic presented in the Fig.8, where harmonic oscillatory motion (pitch or plunge) ($h(\omega t)$) harmonic fluid pressure ($p(\omega t)$) on the solid surface and work done by harmonic aerodynamic forces ($\Xi(\omega t)$) respectively. And ω is the angular frequency and t is the time. Therefore, in the presence of phase lag in the situation where oscillating structure absorbs from surrounding fluid, the

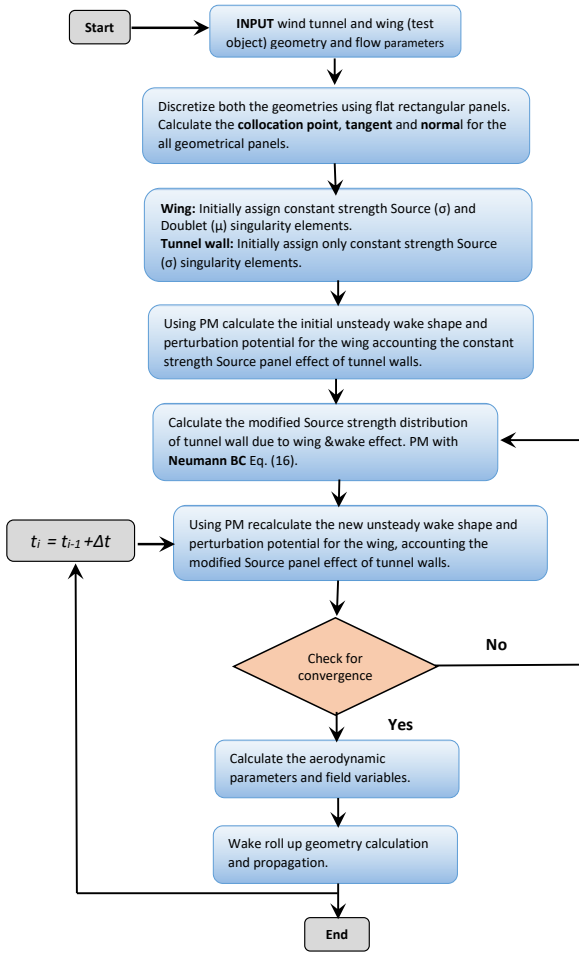


Fig. 7 Flowchart algorithm for wind tunnel wall interference calculation in internal flow using PM

amplitude of oscillation gradually amplifies and leads to flutter or classical flutter as shown in the left column of Fig.8. Whereas in opposite case where structure supplies energy to the surrounding fluid, oscillation amplitude gradually dies out, this kind oscillation termed as damped vibration as shown right column Fig.8. More detailed description of the classical flutter phenomena can be found in [5, 44, 8].

4 Aerodynamic damping calculation

The equilibrium between the structural and aerodynamic forces in the system can be represented by the aeroelastic Eq. (11)

$$[\mathbf{M}]\{\ddot{x}\} + [\mathbf{G}]\{\dot{x}\} + [\mathbf{K}]\{x\} = \mathbf{F}(\ddot{x}, \dot{x}, x, t)_{ad} \quad (11)$$

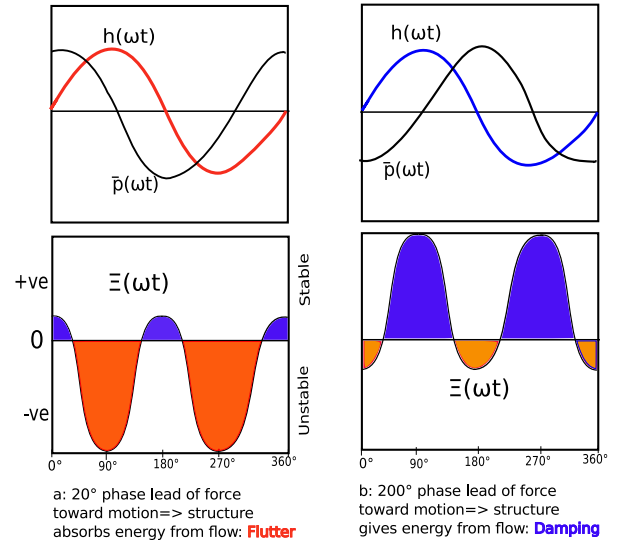


Fig. 8 Schematic illustration of FSI. (a) Flutter: aeroelastically unstable (b) Damped vibration: aeroelastically stable

where $\mathbf{F}(\ddot{x}, \dot{x}, x, t)_{ad}$ can be given by

$$\mathbf{F}(\ddot{x}, \dot{x}, x, t)_{ad} = \mathbf{F}(\ddot{x}, \dot{x}, x, t)_{disturbance} + \mathbf{F}(\ddot{x}, \dot{x}, x, t)_{damping}$$

where $[\mathbf{M}]$, $[\mathbf{G}]$, and $[\mathbf{K}]$ are the modal mass, damping and stiffness matrices respectively, $\{x\}$ represents the modal coordinate vector and $\mathbf{F}(\ddot{x}, \dot{x}, x, t)_{ad}$ is the modal unsteady aerodynamic force vector which contains two terms: $\mathbf{F}(\ddot{x}, \dot{x}, x, t)_{disturbance}$ that includes the aerodynamic disturbances upstream and downstream of the blade and $\mathbf{F}(\ddot{x}, \dot{x}, x, t)_{damping}$ which represents the aerodynamic damping resulting from the interaction between the blade and the flow. For flutter analysis, only the aerodynamic forces due to the vibration of the blade are considered resulting in $\mathbf{F}(\ddot{x}, \dot{x}, x, t)_{disturbance} = 0$ and above Eq. (11) can be simplified into below Eq. (12)

$$[\mathbf{M}]\{\ddot{x}\} + [\mathbf{G}]\{\dot{x}\} + [\mathbf{K}]\{x\} = \mathbf{F}(\ddot{x}, \dot{x}, x, t)_{damping} \quad (12)$$

Solution of the above equation Eq. (12) allows the determination of the aerodynamic damping and thus the aeroelastic stability of the system. The solution of the Eq. (12) similar to that of presented by [9]. However, here the perturbation time varying pressure to oscillation motion is estimated using 3D unsteady PM.

There are different numerical methods which can be used to approximate the aerodynamic characteristics of the system. One of them is ‘‘Time Linearized Method’’ which assumes that the unsteady perturbations in the flow is small compared to that of the mean flow. Then the unsteady flow can be approximated by small harmonic perturbations around a mean value. The details

are presented by Prasad et al.[8]. Thus, the work per oscillation cycle (T) can be obtained by integrating the force and motion during the cycle and can be given by

$$W_{cycle} = \int_{t_0}^{t_0+T} \int_A -p \mathbf{V} \cdot \mathbf{n} dA dt = \int_T \hat{\mathbf{F}} \cdot \hat{\mathbf{h}} \cdot e^{i\omega t} dt \quad (13)$$

where $\hat{\mathbf{h}}$ is the complex motion of the cascade blade. In the present case only pitching motion of the cascade blade is analyzed therefore, it corresponds to torsion motion, thus the yield of the above integral Eq. (13) can be written more explicit form as below

$$W_{cycle} = \pi |\alpha_{tor}| \cdot |m_{pitch}| \cdot \sin(\varphi_{m_{aero} \rightarrow h}) \quad (14)$$

where α_{tor} is the torsional motion amplitude, m_{pitch} aerodynamic moment around pitching axis, respectively. Therefore, aerodynamic damping parameter is given by work done per cycle and normalized by π and amplitude of oscillation "A" and is given in Eq. (15)

$$Aerodynamic\ damping(\Xi) = -\frac{W_{cycle}}{\pi A^2} \quad (15)$$

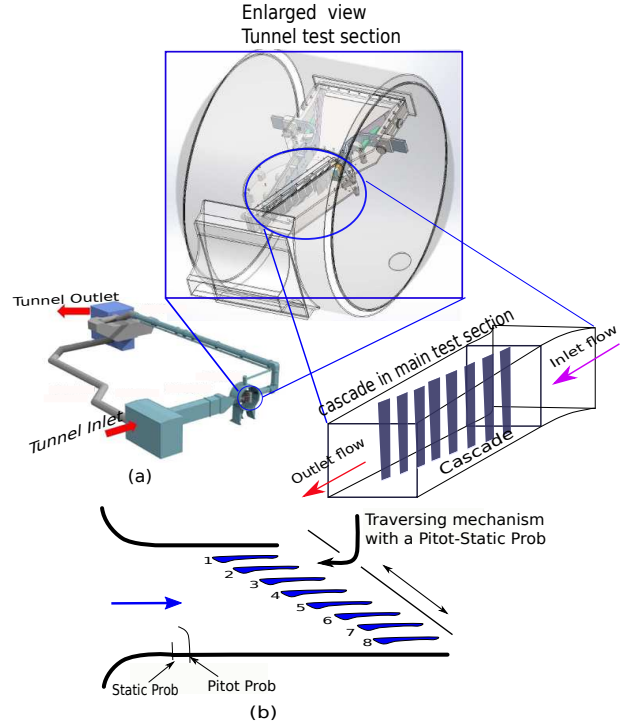
The *positive* value of Ξ indicates the flow acting in stabilising manner whereas *negative* value can cause flutter, therefore, unstable.

5 Reduce order aeroelastic model (ROAM) for stability analysis of 3D cascade

In proposed ROAM numerical model loose coupling strategy is applied, thus, both solver runs independently and exchange the data in preset time step to perform aeroelastic co-simulation. The loose couple is designed such a way that the both solvers are independent of each other's mesh strategy. Furthermore, the proposed method is employed for stability analysis of 3D blade cascade and the estimation of aerodynamic damping s-curve (AD vs IBPA). There are two different test cases are selected for this purpose [45, 9]. Both the test cases experiments are performed in two different laboratories. A similar method is also adopted by Prasad et al. [8, 13].

5.1 First test case description: UWB cascade

The experiment is performed on the 8 bladed cascade in the University West Bohemia (UWB) wind tunnel, Pilzen, Czech Republic by Slama et al. [45, 46]. The test rig and the cascade geometry's are presented in the Fig.9. During the experiment bending and torsional flutter cases are studied and the data is collected for



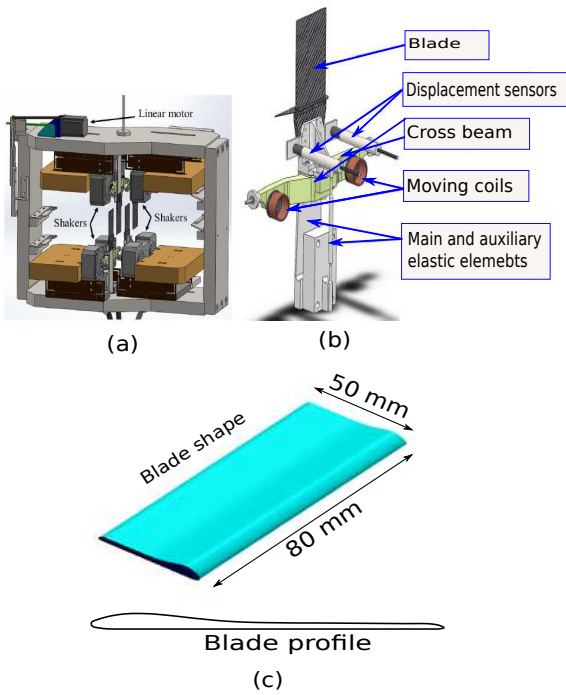


Fig. 10 UWB linear cascade test setup (a) blade and shaker assembly (b) Elastic suspension (c) Blade geometry. [45]

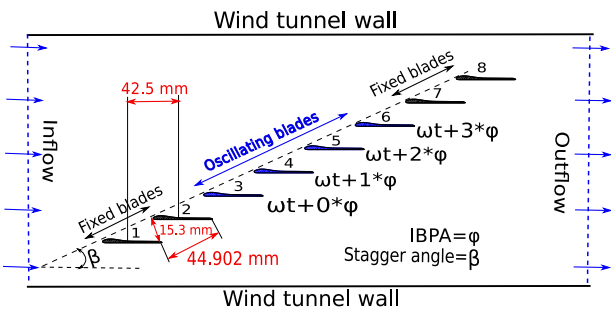


Fig. 11 UWB linear cascade oscillating sequence in TWM mode

315 mated aerodynamic damping using PM on four mid blades (3-6) are compared with experimental and CFD results presented by Slama et al.[45] and [46] for torsional flutter test case. In the PM numerical model, all 335 the 8 blades are discretized using 3D constant strength source and doublet surface panels and the tunnel wall is discretized using only constant strength source panel to simulated the wall effect. Each blade is discretized into 50×25 (chord x span wise) singularity panels and 340 the wind tunnel wall is discretized using 600 flat source panel, the entire grid strategy used in PM numerical model is given in the Fig.12, (fourth wall grid is not shown in the figure due to visibility reason, but it is considered in the calculation). Furthermore, free wake 345 technique is adopted for unsteady wake modeling.

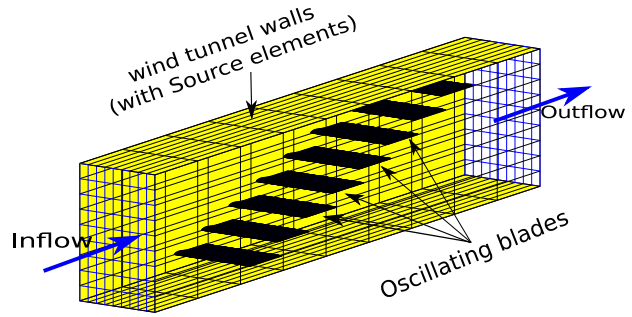


Fig. 12 Grid strategy of direct wall method PM numerical model of UWB test cascade

330 **Modification of blade geometry:** Prior to the discretization a slight modification is made near the trailing edge of the original UWB blade geometry and modification is presented in Fig.13. The key argument for this modification is to use of PM-ROAM solver which assume that there are no flow separation from

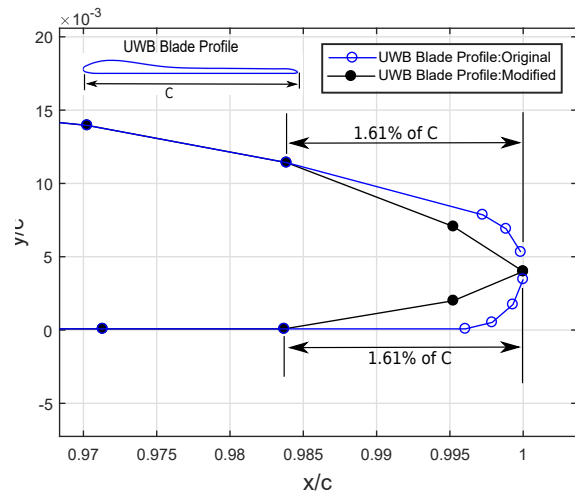


Fig. 13 Modification of UWB blade's trailing edge profile for PM-ROAM

the body surface and the flow must leave body smoothly from the sharp trailing edge of the airfoil. And this is ensured by imposing Kutta condition at the trailing edge, as mentioned earlier in the sec. 2 in PM formulation. However, in reality it is not possible to have zero thickness at airfoil or wing trailing edge which is the case here for UWB original blade profile. Therefore, if classical PM is employed for flow modeling around wing or airfoil, it is recommended by many researchers to adopt this modification to avoid any abrupt pressure jump at the trailing edge, if the trailing edge thickness of real airfoil is not too large. A similar approach is also

adopted by Katz [20]. In the present case modification is done for 1.61% of the airfoil chord (c) near trailing edge as shown in Fig.13, which inflects very negligible effect on over all accuracy of the result related to aerodynamic forces.

Grid convergence test: The grid convergence analysis is carried out on an isolated UWB blade by changing both span wise and chordwise panel numbers. The steady lift coefficient (C_L) at 0.5° incident angle is chosen to be the grid convergence study parameter. Thus, the grid converged for 50 chordwise and 25 spanwise grid panels distribution. The numerical strategy for flut-

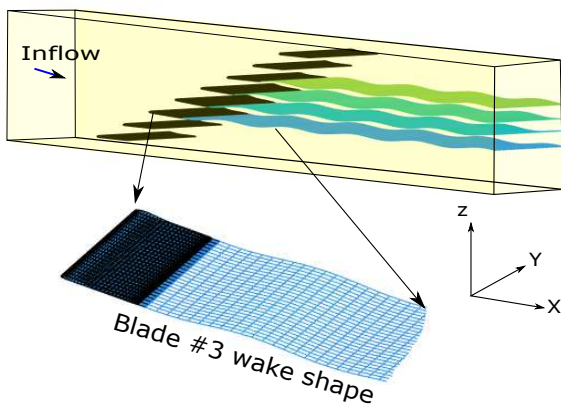


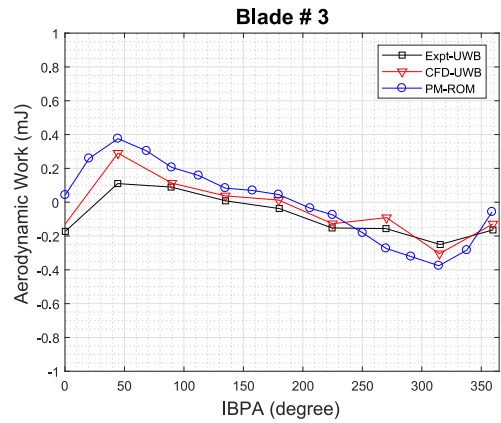
Fig. 14 UWB cascade wake shape of oscillating blade #3

ter simulation is similar to the method presented in the sec 2 accompanied by direct wall method.

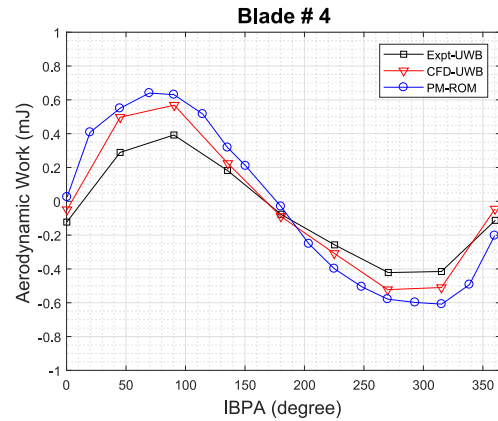
For the transient simulation setup parameters, the time period in the unsteady simulation is defined as the reciprocal value of the tuned frequency ($1/82.2$ Hz). The time step ($\Delta t = 6.0827 \times 10^{-04}s$) was determined on the basis of the total number of time steps per period which was set as 20, a total of 6-time period is simulated to ensure the convergence of the aerodynamic parameters and unsteady wakes. However, the solution starts to converge after 3-time period and the aerodynamic work(AW) value is time averaged to obtain the work per cycle. The wake shape from the blade # 3 in side the wind tunnel is shown in the Fig.14.

In the Fig.14 the simulated unsteady wake shapes from four oscillating blades look reasonably correct and thus, proposed flow solver manage to capture the tunnel wall effect successfully. This can be noticed in the enlarged wake shape of blade -3, there are not any noticeable tip vortices present on the either end of the blade wake, which is as expected because the zero wall clearance is assumed at the both end of the blade in the PM model which makes the flow field inside the tunnel quasi-3D.

In the simulation 0 to 360 degree IBPA is simulated with 20 degree intervals. The aerodynamic moment is estimated for all the four oscillating blades. The aerodynamic work per cycle is then calculated for the torsional flutter using the aerodynamic moment and the definition of the torsional oscillation. The AW(mJ) against IBPA curve is evaluated for the all four oscillating blades using reduced order flow solver and compared with CFD results and experimental data provided by [45, 46]. The results are presented in the Fig.15 and Fig.16. In the Fig.15 and Fig.16 the simulated aerody-



(a)



(b)

Fig. 15 Comparisons of Aerodynamic work(mJ) vs IBPA ; PM-ROAM vs Experimental and CFD(CFX) (a)#3 (b) #4 : Torsional flutter

dynamic work vs IBPA curve using ROAM model shows good agreement with experimental and CFD(CFX) results for all 4 oscillating blades for the torsional flutter. However, ROAM has slightly over estimated the AW compared to experimental as well as CFD(CFX) which can be noticed in all four blades, this is due to inviscid nature of the PM solver.

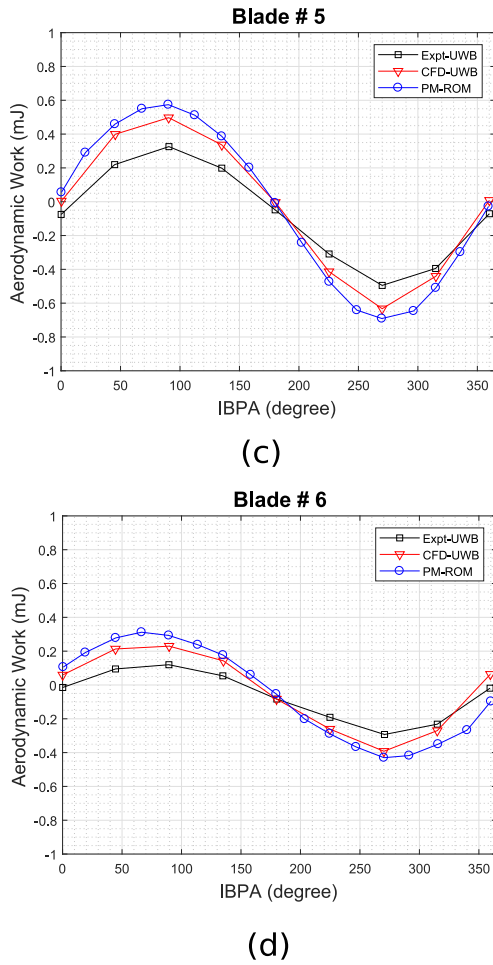


Fig. 16 Comparisons of Aerodynamic work(mJ) vs IBPA ; PM-ROM vs Experimental and CFD(CFX)(a)#5 (b) #6 : Torsional flutter

Furthermore, it is reported by [45] the computational efficiency of CFD(CFX) model for current test is about 1 CPU hour for steady-state(std) simulations on twenty-core 3.10 GHz system. The computational time for unsteady (Ustd) simulations on the same machine is about 16 hours for 6 period for each φ , whereas ROAM-PM model takes 3 minutes for the steady simulation and 11 minutes for unsteady simulation for each φ for 6 period. The computational time comparison between CFD(CFX) and ROAM-PM numerical model is presented in the table.1. Thus, it is clear from the table.1 that there is significant reduction in the computational time when compared to the CFD model for the current test case with similar simulation setup. Also the accuracy of the result is closely comparable with CFD(CFX) numerical model.

Table 1 Computational time comparison: 1st case

| Parameters | PM-ROAM | CFD-Vis |
|------------------|--------------------|-------------------|
| Processor | 1 Core-i7 | 20 Core-i7 |
| Time (cpu):Std | 3 mins | 1hrs |
| Time (cpu):Unstd | 11 mins/ φ | 16 hrs/ φ |
| IBPA-Rang | $\pm 180^\circ$ | $\pm 180^\circ$ |
| IBPA-Interval | 20° | 30° |

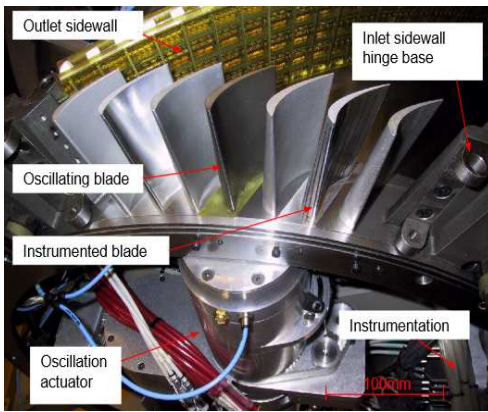
5.3 Second test case description: KTH cascade

In this section the brief description of second test case's experimental setup and the details about numerical modeling of same using unsteady ROAM-PM is presented. The flutter experiment is carried by [9] in 2005 on non-rotating 3D annular cascade section in KTH university's turbomachinery test facility. The annular cascade is consist of 7 blades and the whole setup is presented in Fig.17 and the schematic diagram of test setup is presented in Fig.18. In the 3D cascade setup middle blade is fitted with oscillating actuator to perform controlled oscillation and the second neighboring blade is instrumented with measurement sensors as shown in the Fig.17. The variable inlet and outlet ducts can be move to adjust to set the inflow and outflow angles Fig.18. The coordination convention of the blade profile and flow angle is given in the Fig.19 and the same is adopted in the numerical model of PM solvers. Evaluation of AD is carried out in influence coefficient (INC) method for the torsional and axial bending flutter for different flow conditions. However, in this only torsional flutter case is selected for the validation purpose here. The main flow conditions are (1) nominal inflow angle (α) = -26° and (2) Mach=0.21 and (3) k=0.1 (4) Oscillation type = Torsional. Unsteady pressure and the aerodynamic damping vs IBPA is measured on the instrumented blade Fig.17. More details about blade dimensions and the test setup can be found in [9].

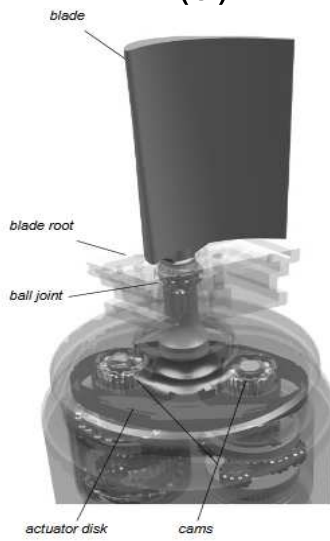
5.4 Numerical model of the KTH cascade test case

The PM discretization and solver method is similar to the first test case. The strategy to include the wind tunnel wall effect is same as in first test case which is represented in flowchart Fig.7.

Modification of blade geometry: Similar to the first test case prior to the discretization a slight modification also is made near the trailing edge of the original KTH blade geometry and it is shown in the Fig.20. And the key argument is same as the first case. A detailed study about effect of trailing edge geometrical shape on PM estimation is carried out by Ezquerro (2017) [47] in his PhD work and also by [48].



(a)



(b)

Fig. 17 Experimental setup of KTH 3D blade cascade and oscillation mechanism [9]

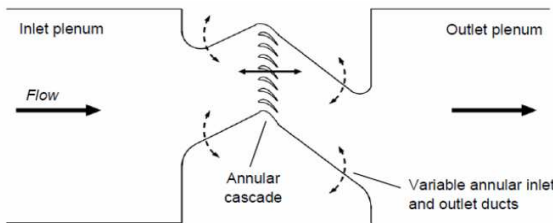


Fig. 18 Schematic diagram of KTH cascade test setup [9]

Grid generation strategy: Though the fundamental numerical strategy of this test case is similar to the first test case (UWB cascade), A significant difference present in the KTH test grid. The complex geometry of KTH test case poses extra challenge of flow leakage from the tunnel wall at the turning while using internal PM method. To mitigate the flow leakage

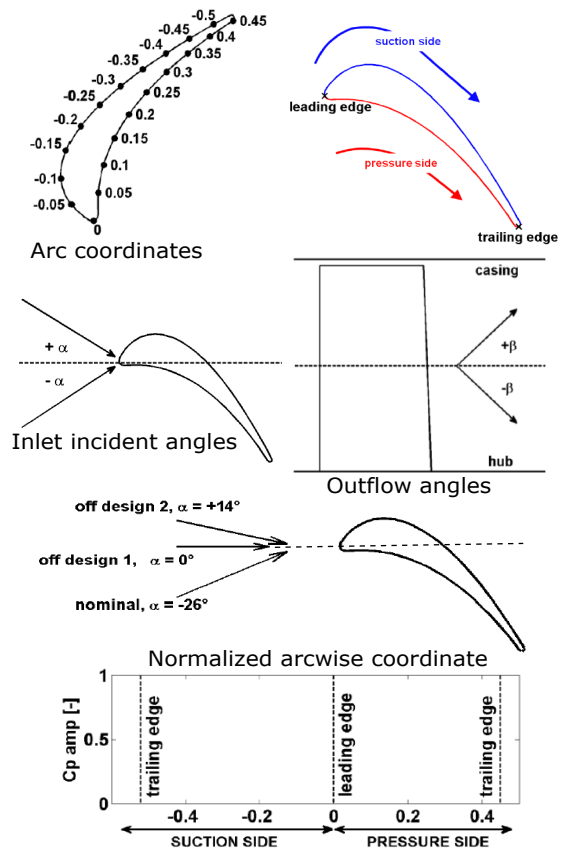


Fig. 19 KTH cascade coordinate conventions [9]

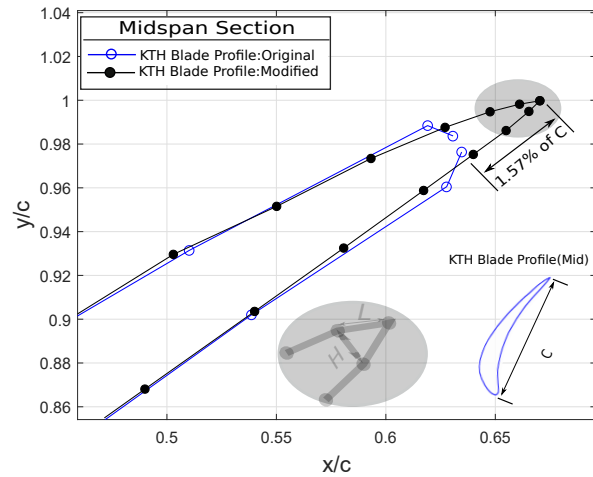


Fig. 20 Modification of KTH blade's trailing edge profile for ROAM-PM and Thickness-ratio (H/L)

466 through the tunnel wall extra effort is required in grid generation.

470 The PM mesh of the KTH cascade and test section of the tunnel is shown in the Fig.21. In the numerical model a part of tunnel geometry is considered starting from variable annular inlet duct till variable annular

outlet duct as shown in the Fig.21(a). The KTH wind

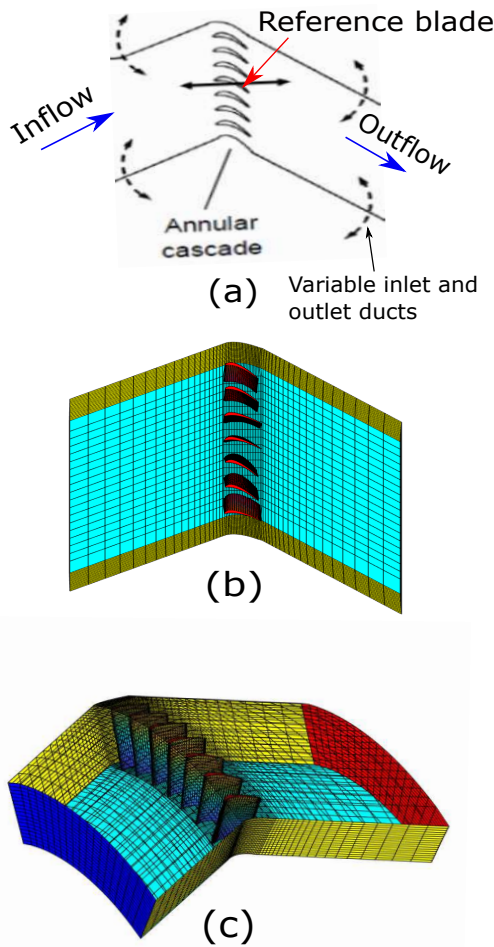


Fig. 21 PM numerical model of KTH tunnel and cascade

tunnel geometry complex with turns and more susceptible for wall leakage while using source PM [34]. Therefore, the KTH test section is discretized into 3D flat rectangular panels with varying mesh densities. Each blade is discretized into 50 (chordwise) \times 16 (spanwise) panels, whereas, all tunnel geometry along with inflow and outflow face are discretized into 11458 3D rectangular panels and the entire mesh is presented in the Fig.21(c).

Furthermore, the wall leakage can also be caused by higher levels of volumetric blockage, which in the present can happen at blade root (hub section) and the tip section (shroud section). Therefore, one of the techniques to significantly minimize the panel wall leakage through tunnel wall is to have sufficiently fine mesh around these area and here it is close to root and hub and the sharp turning of the tunnel. A similar approach is adopted by [34, 35] to minimize the large leakage

issue, thus, similar approach is adopted here as well. In the present model a non-uniform distribution of the panels was used. The mesh density of entire wind tunnel geometry optimized such way that leakage should not be more than 0.5% of the inflow mass flux. The optimized wind tunnel test section mesh strategy is presented in the Fig.22 and the same is used in further numerical simulations. Another aspect of the tunnel wall

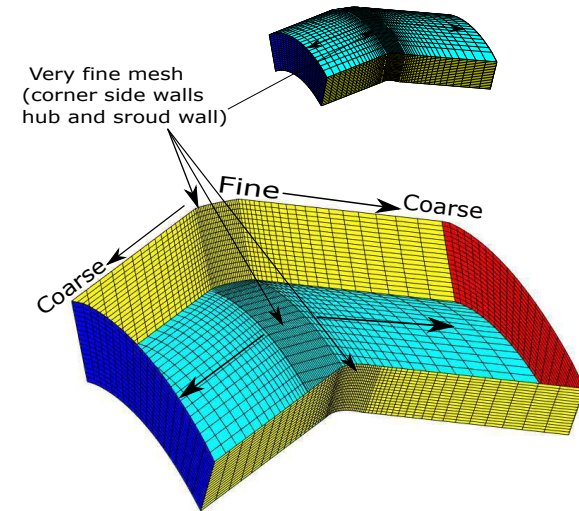


Fig. 22 Mesh strategy for PM numerical model of KTH tunnel and cascade

effect estimation is the orientation of the surface normal on the tunnel wall and test section as described in the subsection 2.1. For this test case the similar approach is adopted and the surface normal strategy is of KTH test geometry is presented in the Fig.23. In the Fig.23 (a) the surface normal of all setup is presented, where, only reference blade is normal shown for better visual clarity. In the Fig.23 (b) the normal orientation blade surface is shown which oriented outwards because the flow of interested is outer surface of the blade, whereas, in wind tunnel's perceptible flow of interest is confined inside the tunnel, therefore, the tunnel wall surface normal is oriented inwards as shown in the Fig.23 (c). The details about this approach is described in the subsection 2.1.

Grid convergence test: The experimentally measured steady pressure coefficient (C_p) distribution at 50% of the span wise position is selected for the grid convergence check. The estimated steady chord wise C_p distribution at 50% at nominal OP for different grind density is compared with experimental C_p and shown in the Fig.24 In the Fig.24 it is clear that estimated C_p using solver start to converge at 50 chord wise and

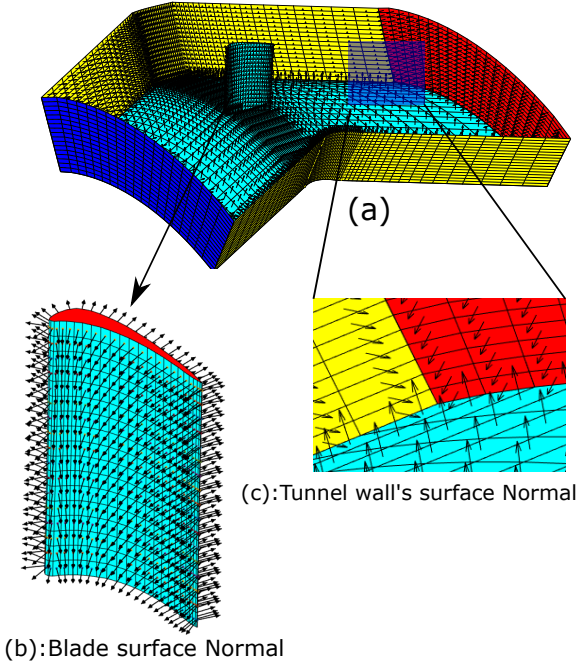


Fig. 23 Wind tunnel wall and reference blade normal (\mathbf{n})

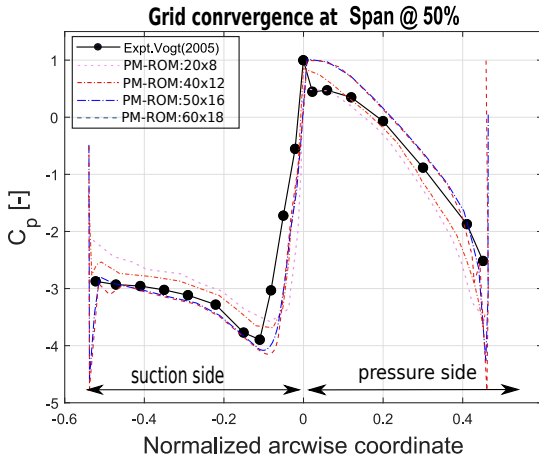


Fig. 24 Grid convergence study of KTH cascade for different value chord wise and panel wise panel numbers.

16 span wise panel distribution. Further, refinement increase computational time and waviness of C_p curve around trailing edge .

Simulation setup description: In the next step constant strength source singularity elements are distributed on each panel of the optimized panel grid of wind tunnel geometry. The combination of constant strength doublet and source elements are chosen to distribute over blade panel grid. The main reason behind selecting these type of element distribution is described in the sec 2. In contrary to Vogt [9] experiment, the

present simulation is carried out in TWM oscillation. As mention earlier in the introduction section in principle the AD curve estimated using both the INC and TWM method's should be identical. Furthermore, torsional flutter case at nominal operating point (OP) for two different $k = 0.1$ and $k = 0.3$ is simulated. Since the values of k is low, therefore, for the present 3D annular cascade method of linear superimposition can be considered to include the effects of neighboring oscillating blades on the reference blade. Other simulation flow conditions are similar to the chosen test case given by [9]. Both steady and unsteady simulation is carried out to estimate the aerodynamic stability parameter and pressure coefficient (C_p) distribution over blade surface. Only 1% tip clearance (blade span) case is considered in the PM model simulation. For the unsteady simulation setup parameters, the time period (T) is defined as the reciprocal value of the tuned frequencies (for $k=0.1$, $f=23$ Hz, $T=1/23$ sec and for $k=0.3$, $f=69$ Hz, $T=1/69$ sec) and the respectively, time step (for $k=0.1$, $\Delta t = 0.0022s$ and for $k=0.3$, $\Delta t = 7.2464 \times 10e - 04s$) was determined on the basis of the total number of time steps per period which is set to be 20, total 6-time period is simulated to ensure the convergence of the aerodynamic parameters and unsteady wakes, however, the solution start to converge after 3rd and 4th time period (T) respectively. Then the aerodynamic work (AW) value is time averaged to obtain the work per cycle.

Results and discussion: AT first the ROAM-PM estimated steady chordwise C_p distribution over the reference blade at three different spanwise position is compared with experimental data by [9] and presented in the Fig.25, Fig.26 and Fig.27. At the first glance in Fig.25

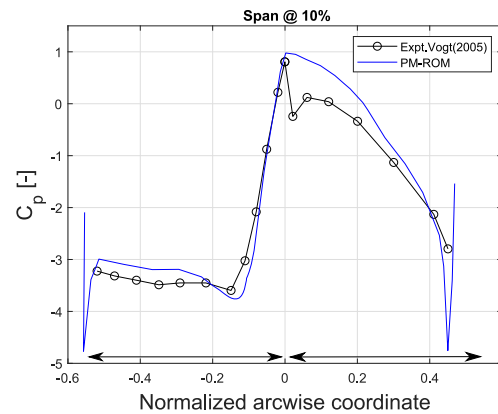


Fig. 25 Steady C_p distribution at 10% spanwise position; low subsonic, nominal inflow OP

it can be noticed that the estimated C_p using PM numerical model has reasonably close agreement with the

experimental results for the low subsonic nominal flow case. However, close to leading edge on the pressure side simulated and experimental has C_p between arc=0 till arc=0.05 shows significant discrepancy. It is important to mention that sharp dip in experimental C_p at this position caused by local flow separation bubble formed close to root section of the blade due to blade's higher thickness and geometrical twist, and it is well highlighted by Vogt [9] in CFD results. The schematic representation of the leading edge separation bubble structure is presented in the Fig.28 However, the present nu-

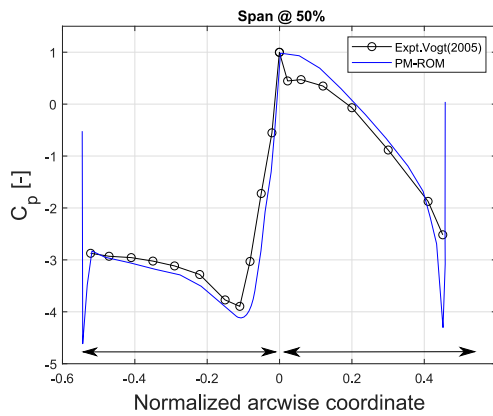


Fig. 26 Steady C_p distribution at 50% spanwise position; low subsonic, nominal inflow OP

merical flow solver, based on the underlying principle of potential flow unable to capture the flow separation or separation bubble, thus, over estimate the C_p value in the leading edge region of pressure side.

In the Fig.26 steady pressure loading C_p at 50% spanwise position is compared with measured data, show fair agreement between two results. However, the disagreement of C_p close to the leading on the pressure side observed, and the reason for this is same as 10% case. However, in comparison to 10% case in Fig.25, the difference in 50% case is less. As we move from root to tip section of the blade, the twist decreases and accompanied with annular shape of the cascade, the flow incident angle became less negative (according the present angle convention Fig.19), thus, the size and strength of local separation bubble close to the leading edge of pressure side decreases Fig.28, consequently smaller pressure drop at 50% compared to at 10%. Therefore, the estimated C_p is much closer to measured one at this position Fig.25.

Next, in the Fig.27 estimated C_p is compared with the measure data at 90% spanwise position close to the blade tip. Though RAOM-PM solver estimates the C_p value at 90% spanwise position is close to the measure

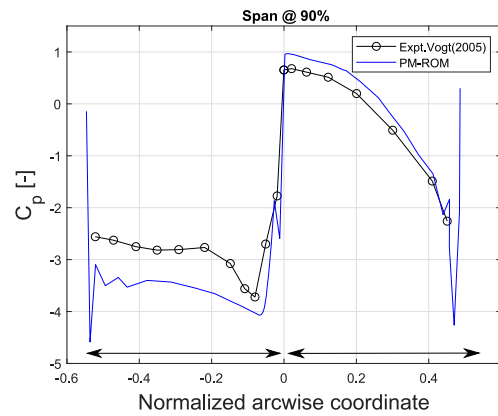


Fig. 27 Steady C_p distribution at 90% spanwise position; low subsonic, nominal inflow OP

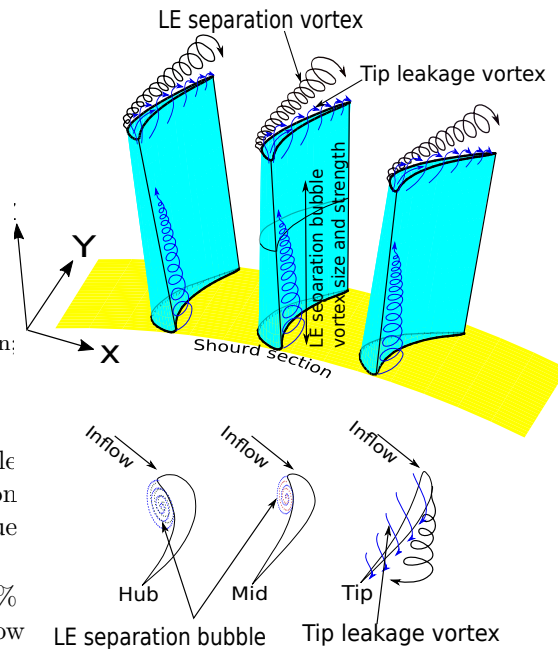


Fig. 28 Schematic representation of axial vortex and tip leakage in 3D blade cascade

C_p at pressure side, the agreement between results are not as good as for 10% and 50% case. Furthermore, in the Fig.27 the estimated C_p in the pressure side is relatively closer to measured data compared to the suction side. A significant diversion can be notice in the suction side. Also there are significant oscillation is present in the C_p magnitude, largely near the trailing edge of the profile along with the slight overestimation of peak suction pressure in ROAM-PM results can be noticed. Close to the tip blade loading is reduced in comparison root due to increase negativity of incident aoa cause by geometric twist as shown in the Fig.28. Also mild separation shear layer detached aft of the leading edge on suction side as shown in the Fig.28. Moreover, the vor-

ticity strength of tip section is further intensified by tip leakage vortices as shown in the Fig.29. This secondary flow near the tip yield of combined effect of leading edge separated share layer and tip vortices believed to be because of reduction of the pressure on the suction side at 90%. The drop in pressure increase from leading edge to trailing edge in the downstream direction as the strength of vortices grows Fig.29. Also in the present case 1% tip clearance is considered, therefore, a significant interaction between tip leakage secondary flow and the shroud wall can happen, this might also be the cause of drop in pressure near the tip at suction side. Since the can not model secondary complex flow thus, overestimate the C_p vale near tip section. Perhaps more sophisticated flow model is require to accurately capture such flow field. However, PM results close to tip can be improved by modeling of close tip as presented in top sub-figure of Fig.29. But in the present case this approach dose not significantly improves te result, but increase the computational time. Therefore, in the present research tip is left hollow.

Furthermore, the large spike can be observed in all estimated C_p value close to trailing edge in the three positions, also at 90% position significant oscillation present in the C_p close the trailing edge Fig.27. This is due to ROAM-PM solver characteristics, solutions based on the Dirichlet boundary condition(present PM method) which suffer from this problem when the trailing edge is very thin [48, 11]. The trailing edge thickness parameter can be defined as H/L , where H is the distance between the upper and lower trailing edge collocation points and L is the chord of the trailing edge panel as shown in the Fig.20 schematically. A satisfactory result can be obtained as long as $H/L > 0.25$, below this value Dirichlet-based PM can become inaccurate near the trailing edge. For the modified KTH airfoil the value of the thickness parameter at the 10% is $H/L = 0.173$ and it decreases as move towards the tip section. Therefore, a sudden spike can be observed close to the trailing edge on both suction side(SS) and pressure side(PS) and the magnitude of spike increase towards the tip. At 90% the the airfoil trailing edge very thin which also cause the waviness in the C_p value along with large spikes. However, by moving the panel more further this problem can be solved, but in this case the geometry will be effected significantly, Therefore, it is kept close to the original shape here.

The 3D velocity streamline around the blade#0 for ROAM-PM steady state simulation is plotted using MATLAB R2019b *Stream3* function and is given in the Fig 30. The streamline plot in the Fig.30 indicates the PM fails to capture the leading edge separation bubble effect as it is clear in the sub Fig.30(b). Further-

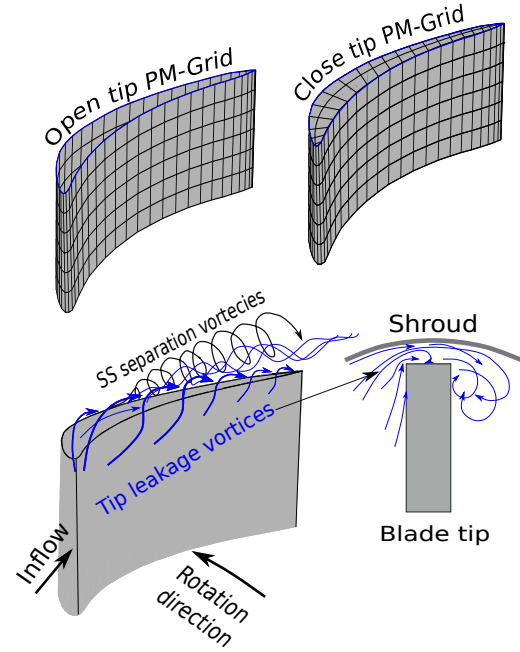


Fig. 29 Schematic representation of tip clearance, tip shapes and tip leakage in 3D blade cascade

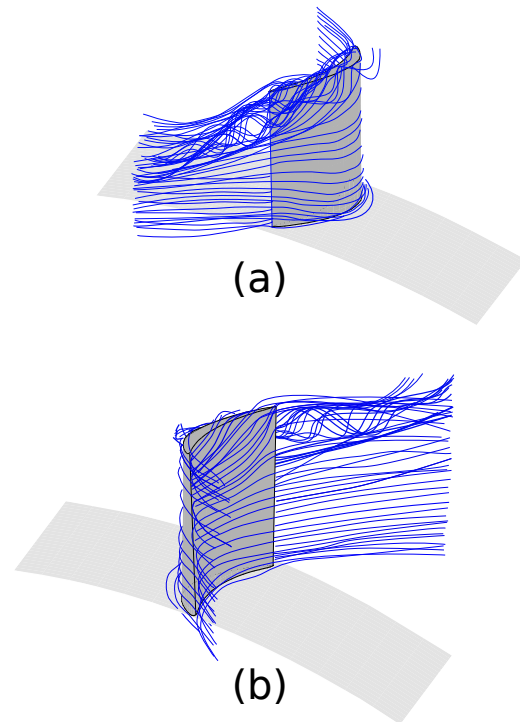


Fig. 30 Schematic representation of tip clearance, tip shapes and tip leakage in 3D blade cascade

more, the PM has manage to capture the tip leakage and shroud wall interaction with secondary flow close to the tip in some extent, but, entirely fails to simulate the leading edge separation in the suction of the blade which is schematically presented in the sub

Fig.30(a). Thus, the 3D stream line plots also confirms the ROAM-PM inability to simulate any separated flow. The streamline calculation is performed using MATLAB-R2019b *Stream3* function and it is computationally expensive ROAM-PM solver. However, modified version of PM can be employed to simulate the flow separation as proposed by [11]. Since the current research work is focused on classical flutter, therefore, separated flow model is out of its scope, and thus, not reasonable to consider in the flow model.

Unsteady Results: Unsteady results are compared and presented here for nominal OP (L1) $k=0.1$. To keep the results aligned with Vogt's results the data is also presented in same fashion as of Vogt in the form of absolute C_p magnitude and phase (± 180 deg). The estimated absolute amplitude of the unsteady pressure coefficient (C_p) and phase value for torsional flutter case at nominal OP(L1) is compared with experimental data at three spanwise position similar to that of steady case for blade 0 and blade -1. However, for the blade 0 measurement is done only at mid span (at 50%), therefore, for the blade 0 only mid span estimated values are possible to be compared here. Thus, in the Fig.31 estimated unsteady C_p and phase at 50% on the blade 0 is compared against experimental measurement. In the Fig.31

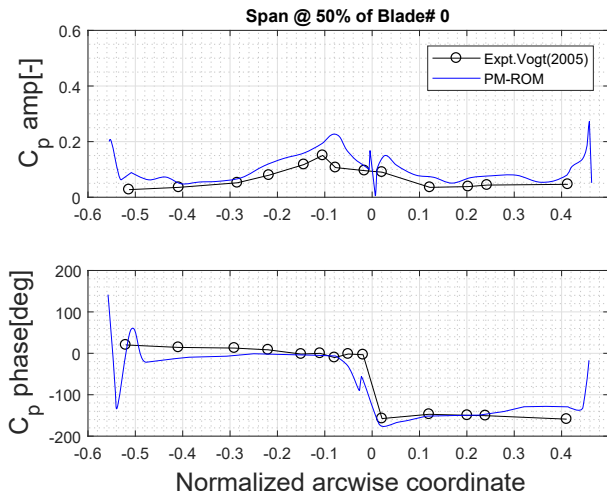


Fig. 31 Comparison of measured and predicted unsteady response on blade#0 at mid span for torsional mode flutter; low subsonic, nominal inflow OP, $k=0.1$

estimated unsteady C_p amplitude and phase on both suction side (SS) and pressure side (PS) shows good agreement with experimental results. However, sharp peak is observed close to trailing edge for the C_p and phase curve. This is believed to be for the same reason as explained in the steady case, inherent problem of Dirichlet BC if thickness ratio $a < 0.133$. Further-

more, the oscillation and slight overestimation close to leading edge is caused by leading edge local moving vortices present in the flow due to geometrical twist of the blade. The classical ROAM-PM can not model local flow separation, thus, overestimates C_p and oscillation is caused by movement of these vortices due to torsional motion of the blade.

A similar comparison of unsteady C_p and phase for blade -1 at three spanwise positions 10%, 50%, and 90% is presented in Fig.33, Fig.32 and Fig.34. In the Fig.32 estimated C_p shows good agreement with experimental results. However, the leading edge oscillation persists in all the results. Furthermore, the estimated

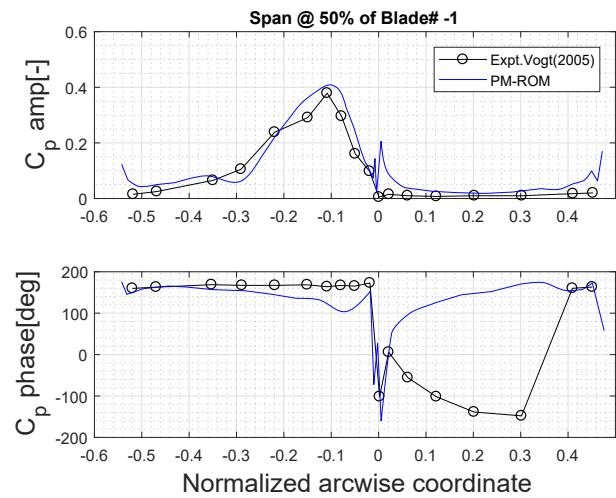


Fig. 32 Comparison of measured and predicted unsteady response on blade -1 at mid span for torsional mode flutter; low subsonic, nominal inflow OP, $k=0.1$

response phase value in the suction side is very close to the measured, but at the PS large diversion in response phase value can be observed. In the Fig.33 ROAM-PM estimated C_p and response phase at 10% is compared. The estimated result shows similar behavior like mid span position. In this position unsteady C_p amplitude and response phase (SS) has close agreement with experimental data, however, the response phase diverges significantly in the PS. Perhaps the unsteadiness of response phase can not be well captured by inviscid solvers like PM.

In the Fig.34 same parameters are compared at 90% span position close to the blade tip. The estimated C_p and the response phase results show significant diversion from the measured data at this position. However, the estimated unsteady C_p is close to experimental results in the PS, but in the SS is not satisfactory and this is also true for the response phase value on both sides. Close to the tip flow field is dominated by the tip

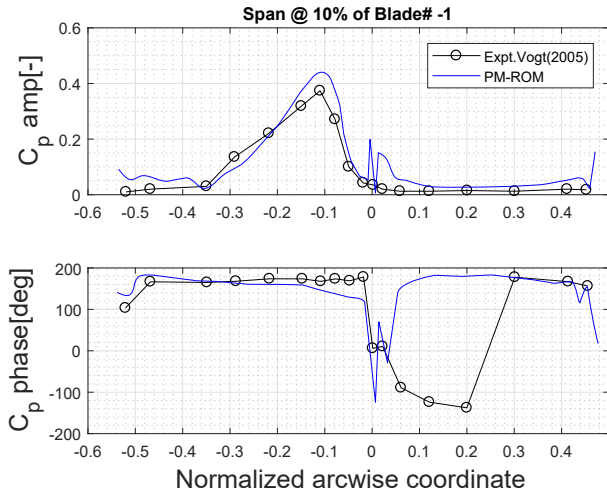


Fig. 33 Comparison of measured and predicted unsteady response on blade# -1 at 10% span for torsional mode flutter; low subsonic, nominal inflow OP , $k=0.1$

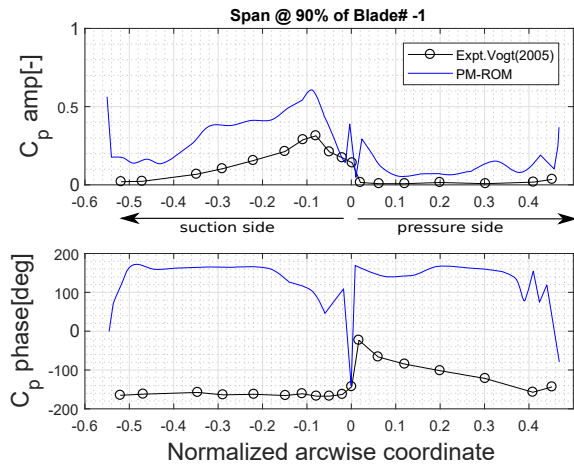


Fig. 34 Comparison of measured and predicted unsteady response on blade -1 at 90% span for torsional mode flutter; low subsonic, nominal inflow OP , $k=0.1$

leakage vortices and also leading edge separation shear layer due to higher incident angle. Therefore, the flow field at 90% position is highly nonlinear and can not be represented by classical ROAM-PM. An advance model might be needed.

Furthermore, the solver is employed to estimated the aerodynamic stability parameters of torsional flutter case in TWM at low subsonic nominal flow condition. The simulation is carried out between -180° to $+180^\circ$ IBPA angle with the interval of 20° for two different reduced frequencies ($k=0.1$ and 0.3). The simulated AD vs IBPA curves for reference blade is compared with experimentally estimated AD by [49] and presented in Fig.35 and Fig.36 receptively. The simulated AD using 3D PM flow model at different IBPA for $k=0.1$ agrees

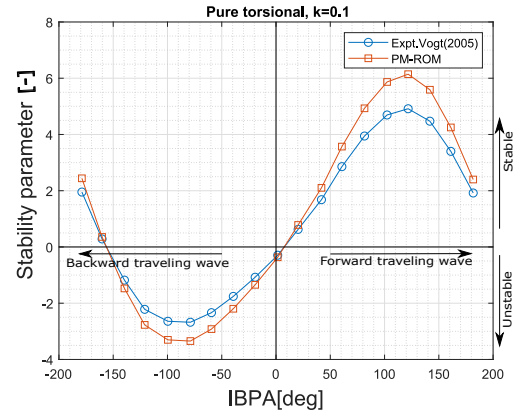


Fig. 35 AD vs IBPA s-curve of reference blade for torsional flutter at low subsonic, nominal inflow OP , $k=0.1$

well with experimental results in Fig.35. The PM based solver has accurately captured the $S - curve$ running from unstable to stable zone, (-180° to $+180^\circ$). However, the PM model overestimates the magnitude of AD values between IBPA -50° to -100° in unstable zone and for IBPA $+100^\circ$ and $+180^\circ$ in stable zone. This is caused by phase lead between unsteady aerodynamic force and period of oscillation at these IBPA.

In the Fig.36 estimated AD vs IBPA curve is compared with measured AD curve for $k=0.3$. The numerical estimated AD vs IBPA curve fairly close with experimental one. However, just like in the previous case ($k=0.1$) solver over estimate the magnitude of AD values around the peak regions in both stable and unstable zone and it can be caused by the same very reason as in the $k=0.1$ case in Fig.36. Apart from this, es-

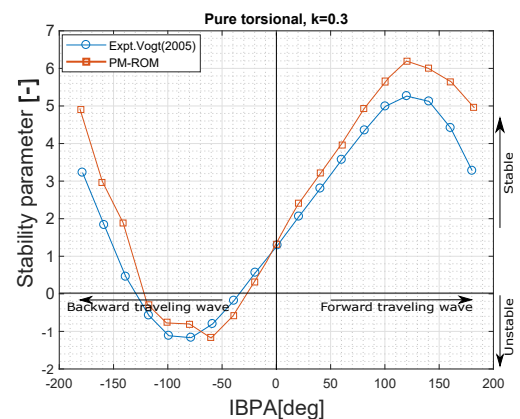


Fig. 36 AD vs IBPA curve of reference blade for torsional mode flutter; low subsonic, nominal inflow OP , $K=0.3$

timated AD curve for $k=0.3$ is not as smooth as for $k=0.1$ case. Though it is qualitatively representative, but shows waviness in pattern compared to experimen-

tal one. This effect can be explained by the effect of reduced frequency which is increased to $k=0.3$ in the later case. The present numerical scheme is more suitable for classical flutter type of problem in turbomachinery (where $k < 0.3$) to better application of superimposition principle. However, if flow field is very unsteady around the blade cascade then it is very challenging to apply the superimposition principle effectively. At $k=0.3$ the flow field around the cascade is quite unsteady or non linear, therefore, the solver can not estimate the AD value accurately and consistently for all IBPA and can cause waviness in AD. Therefore, the s-curve looks non smooth in compared the $k=0.1$ case.

Furthermore, the overestimation of numerically estimated AD values around peak value of the curve at above mentioned IBPA for the given flow condition cause by mild flow separation from the suction side of the blades, since current version of ROAM-PM can not simulate the separated flow, thus, overestimate the magnitude of the AD values at those IBPA. Also the effect of acoustic resonance can not be denied. Since there is no flow separation or acoustic resonance model implemented in the present version PM flow solver, therefore, it overestimates the AD magnitude values. Therefore, to deeply understand the involved complex secondary flow phenomena and to find out the root cause of the overshoot of AD values, a detailed CFD based (higher fidelity model) analysis will be required which is computationally very expensive. Nevertheless, the AD results are accurate enough to be used for preliminary design stage and the computational time which is way less than the computational time taken, if CFD based models have been adopted for the simulation purpose. The computational time between ROAM-PM and the CFD based numerical model is presented in the table.2

It should be noted, that there is not any informa-

Table 2 Computational time comparison: 2^{nd} case

| Paratmeters | PM-ROAM | CFD-invs |
|------------------|--------------------|---------------------|
| Processor | 1 Core-i7 | 48 Core-i7 |
| Time (cpu):Std | 7 mins | 1hrs |
| Time (cpu):Unstd | 16 mins/ φ | 9.54 hrs/ φ |
| IBPA-Rang | $\pm 180^\circ$ | $\pm 180^\circ$ |
| IBPA-Interval | 20° | 30° |

tion reported about computational time by Votg.[9], but his work is repeated later (numerical part) by [50] and the computational time using CFD is referred from Camera[50] work.

6 Conclusion

The classical flutter phenomena in turbomachinery 3D blade cascade is studied using medium fidelity ROAM which is developed using BEM type PM for flow modeling. The prime goal of the proposed ROAM-PM numerical model is to significantly bring down the computational cost with acceptable accuracy for aeroelastic stability analysis of turbomachinery system. The ROAM-PM is validated against two different test case of made of 3D blade cascade system under controlled flutter experiment.

Both test cases are carried out in subsonic flow domain and control flutter environment. The ROAM-PM estimated aerodynamic work per cycle for given IBPA shows good agreement with experimentally measured results in the first test case. The wind tunnel wall effect is successively modeled using ROAM-PM in the this test case. However, the model marginally overestimate aerodynamic work magnitude compared to measured data for given IBPA. However, for the same CFD-viscous model also overestimate the aerodynamic work results, but lesser extent compared to model. Though the CFD(CFX) numerical results marginally superior and are more close to measured data compared to model, The turn out be way more cost effective in computational time aspect and the models yields are qualitatively well within acceptable accuracy range for the first test case. Therefore, after comparing the aerodynamic work vs IBPA curve and the computational time comparison table for the first test case it is evident that has managed to successfully fulfill its prime objective of computation cost reduction with acceptable accuracy for this test case being an medium fidelity numerical model.

Furthermore, the ROAM-PM is employed to model more complex second test case, which also quasi-annular in nature. Both steady and unsteady loading estimated using is compared with the experimentally measured data for the low subsonic flow case which correspond to the scenario of classical flutter. The ROAM-PM estimated results shows good match with measure data. One of the key challenging part in second test is to model the tunnel wall effect which is contrary to the first test case have much more complex geometry due sharp turning and corners which can cause panel leakage in PM numerical model. However, with proper optimization and adequate modification ROAM-PM has successfully managed to simulate the flow field with desired accuracy. However, there are some discrepancies observed in the results close to tip section of the results and which is mainly cause by the localized secondary flow and separated flow effects. This kind of flow regime is out of scope of classical ROAM-PM, This is main re-

sults are diverging significantly from measured results. More specifically C_p amplitude and phase at the tip section of steady and unsteady results. Furthermore, the estimated aerodynamic damping vs IBPA curve has very good qualitative agreement for the both lower and higher values of reduced frequency in the second test case. However, while comparing computational time of ROAM-PM against high fidelity CFD(CFX) type numerical model for the same test case, the proposed ROAM-PM shows massive lead. Therefore, once again ROAM-PM has proved its capability to fast estimation of aeroelastic stability with desired accuracy for the classical flutter type problems in turbomachinery system.

At the end after a careful scrutiny of the presented results and the performance comparison tables of ROAM-PM with CFD model, it is safe to say that ROAM-PM can be an excellent trade off between computational speed and accuracy for aeroelastic stability analysis of turbomachinery blade cascade. Thus it can be used for aeroelastic instability analysis e.g. classical flutter analysis, limit cycle oscillation etc. Furthermore, the capacity and the accuracy of present ROAM-PM model can further be improved by including viscous-inviscid coupling and acoustic resonance model. Therefore, in the light of above script as an overall conclusion one can safely say that the present ROAM-PM is arguably a versatile numerical tool of aeroelastic instability analysis for turbomachinery application and has successfully managed to reduce the computational time for such coupled calculation in a great extent and without compromising the overall accuracy of the results in comparison to high fidelity models. Thus, it can be a very promising tool in the industrial application for quick aeroelastic design analysis within short period of time compared to high fidelity CFD-CSD tools at the preliminary design stage. However, the application of high fidelity model can not be completely ignored at preliminary design stage where the flow field around the blade cascade is more complex and accompanied with high amplitude oscillatory flutter problem e.g. in transonic flow flutter, separated flow or large amplitude high frequency flutter in cascade (stall flutter case).

Declarations

Acknowledgment

The authors of article acknowledge that portion of this manuscript (Fig.35, some part of second test case) has been presented in the " 15th IFToMM World Congress on Mechanism and Machine Science, 15-18 July 2019,

Krakow, Poland" and same can be cited as Prasad et al. [51].

Funding

This research work is supported by the grant projects with "No. 19-02288J: Robust reduced-order modeling of fluid-structure interaction problems" of the Czech Science Foundation (CSF). This work is also partially supported within institutional support RVO:61388998, and the by the "Center of Excellence for Nonlinear Dynamic Behavior of Advanced Materials in Engineering CZ.02.1.01/0.0/0.0/15_003/0000493 (Excellent Research Teams) in the framework of Operational Program Research, Development". Furthermore, the authors would also like to thank Doosan koda Power s.r.o for providing us the experimental data used in the validations for the first test case. Doosan koda Power s.r.o collaborated with the Institute of thermomechanics in the context of another research project funded by Technology Agency of the Czech Republic (TACR) under the National competence center (NCK) framework No: TN1000007, sub-project V1.7.3: "The procedure for calculating the flutter of long blades", which also partially supported this research work.

Conflict of interest

The authors have no conflicts of interest to declare that are relevant to the content of this article.

Availability of data and material

Not applicable

Code availability

Not applicable

References

1. Nuclear power: 2 largest steam turbine ever made., <https://www.ge.com/news/reports>, accessed: 2020-10-06 (2020).
2. A. V. Srinivasan, Flutter and Resonant Vibration Characteristics of Engine Blades, Journal of Engineering for Gas Turbines and Power 119 (4) (1997) 742–775, doi:<https://doi.org/10.1115/1.2817053>.

3. L. Pešek, M. Hajžman, L. Půst, V. Zeman, M. Byrtus, J. Brůha, Experimental and numerical investigation of friction element dissipative effects in blade shrouding, *Nonlinear Dynamics* 79 (3) (2015) 1711–1726, doi:<https://doi.org/10.1007/s11071-014-1769-3>.
4. F. Brahimi, A. Ouibrahim, Blade dynamical response based on aeroelastic analysis of fluid structure interaction in turbomachinery, *Energy* 115 (2016) 986 – 995, doi:<https://doi.org/10.1016/j.energy.2016.09.071>.
5. T. Fransson, *Aeroelasticity in axial flow turbomachines*, Von Karman Institute for Fluid Dynamics, Brussels, Belgium, 1999.
6. H. Atassi, T. Akai, Effect of blade loading and thickness on the aerodynamics of oscillating cascades, in: 16th Aerospace Sciences Meeting, AIAA 1978, p. 277, doi:<https://doi.org/10.2514/6.1978-227>.
7. J. Panovsky, R. E. Kilelb, A design method to prevent low pressure turbine blade flutter, *Journal of engineering for gas turbines and power* 122 (1) (2000) 89–98, doi:<https://doi.org/10.1115/1.483180>.
8. C. S. Prasad, L. Pešek, Efficient prediction of classical flutter stability of turbomachinery blade using the boundary element type numerical method, *Engineering Analysis with Boundary Elements* 113 (2020) 328–345, doi:<https://doi.org/10.1016/j.enganabound.2020.01.013>.
9. D. Vogt, Experimental investigation of three-dimensional mechanisms in low-pressure turbine flutter, Ph.D. thesis, Kungliga Tekniska Hogskolan(KTH), Stockholm, Sweden, <http://www.diva-portal.org/smash/get/diva2:7902/FULLTEXT01.pdf> (2005).
10. J. L. Hess, Calculation of potential flow about arbitrary three-dimensional lifting bodies, Final Technical Report MDC J5679-01, Naval Air Systems Command, Department of the Navy, <https://apps.dtic.mil/sti/citations/AD0755480> (1972).
11. C. S. Prasad, G. Dimitriadis, Application of a 3d unsteady surface panel method with flow separation model to horizontal axis wind turbines, *Journal of Wind Engineering and Industrial Aerodynamics* 166 (2017) 74 – 89, doi:<https://doi.org/10.1016/j.jweia.2017.04.005>.
12. X. Shen, J. Chen, P. Hu, X. Zhu, Z. Du, Study of the unsteady aerodynamics of floating wind turbines, *Energy* 145 (2018) 793 – 809, doi:<https://doi.org/10.1016/j.energy.2017.12.100>.
13. C. Prasad, Q.-Z. Chen, O. Bruls, F. D'Ambrosio, G. Dimitriadis, Aeroservoelastic simulations for horizontal axis wind turbines, *Proceedings of the Institution of Mechanical Engineers, Part A: Journal of Power and Energy* 231 (2) (2017) 103–117, doi:<https://doi.org/10.1177/0957650916678725>.
14. P. Liu, A computational hydrodynamics method for horizontal axis turbine panel method modeling migration from propulsion to turbine energy, *Energy* 35 (7) (2010) 2843–2851, doi:<https://doi.org/10.1016/j.energy.2010.03.013>.
15. J. feng Tan, H. wen Wang, Simulating unsteady aerodynamics of helicopter rotor with panel/viscous vortex particle method, *Aerospace Science and Technology* 30 (1) (2013) 255–268, doi:<https://doi.org/10.1016/j.ast.2013.08.010>.
16. Y. Cao, S. Lv, G. Li, A coupled free-wake/panel method for rotor/fuselage/empennage aerodynamic interaction and helicopter trims, *Proceedings of the Institution of Mechanical Engineers, Part G: Journal of Aerospace Engineering* 229 (3) (2015) 435–444, doi:<https://doi.org/10.1177/0954410014534203>.
17. W. Sun, G. Huang, Integrated lifting line/surface panel method for optimal propeller design with consideration of hub effect, *Journal of Hydrodynamics* 31 (6) (2019) 1218–1230, doi:<https://doi.org/10.1007/s42241-019-0051-z>.
18. W. Xiaozhe, W. Zhiqiang, L. Zhu, Y. Chao, Integrated optimization on aerodynamics-structure coupling and flight stability of a large airplane in preliminary design, *Chinese Journal of Aeronautics* 31 (6) (2018) 1258–1272, doi:<https://doi.org/10.1016/j.cja.2018.01.024>.
19. M. Rezaei, M. Behzad, H. Haddadpour, H. Moradi, Aeroelastic analysis of a rotating wind turbine blade using a geometrically exact formulation, *Nonlinear Dynamics* 89 (4) (2017) 2367–2392, doi:<https://doi.org/10.1007/s11071-017-3591-1>.
20. J. Katz, A. Plotkin, *Low-Speed Aerodynamics*, 2nd Edition, Cambridge University Press, 2001, doi:<https://doi.org/10.1017/CBO9780511810329>.
21. E. McFariand, Solution of plane cascade flow using improved surface singularity methods, *Journal of Engineering for Power* JULY 104 (1982) 669.
22. Z. Q. Lei, G. Z. Liang, Solution of turbine blade cascade flow using an improved panel method, *International Journal of Aerospace Engineering* (2015) Article ID 312430, doi:<https://doi.org/10.1155/2015/312430>.
23. F. Barbarossa, A. B. Parry, J. S. Green, L. di Mare, An aerodynamic parameter for low-pressure turbine flutter, *Journal*

- of Turbomachinery 138 (5) (2016) 051001, doi:<https://doi.org/10.1115/1.4032184>.
24. R. Ramirez Camacho, N. Manzanares Filho, A source wake model for cascades of axial flow turbomachines, *Journal of the Brazilian Society of Mechanical Sciences and Engineering* 27 (3) (2005) 288–299, doi:<https://doi.org/10.1590/S1678-58782005000300011>.
25. S. H. Chen, Turbomachinery blade loading prediction using the panel method, in: *Boundary Element Methods in Engineering*, Springer, 1990, pp. 29–35, doi:https://doi.org/10.1007/978-3-642-84238-2_5.
26. C. Reis, N. Manzanares-Filho, A. De Lima, Robust optimization of turbomachinery cascades using inverse methods, *Journal of the Brazilian Society of Mechanical Sciences and Engineering* 38 (1) (2016) 297–305, doi:<https://doi.org/10.1007/s40430-015-0309-5>.
27. N. Manzanares-Filho, C. A. A. Moino, A. B. Jorge, An improved controlled random search algorithm for inverse airfoil cascade design, *Proceedings of the 6th World Congresses of Structural and Multidisciplinary Optimization*, Paper (4451).
28. K. Yiu, Computational methods for aerodynamic shape design, *Mathematical and Computer Modelling* 20 (12) (1994) 3 – 29, doi:[https://doi.org/10.1016/0895-7177\(94\)90121-X](https://doi.org/10.1016/0895-7177(94)90121-X).
29. W. Yang, Three-dimensional inverse method for aerodynamic optimization in compressor, in: *IOP Conference Series: Materials Science and Engineering*, Vol. 52, IOP Publishing, 2013, p. 012008, doi:<https://doi.org/10.1088/2F1757-899x2F522F12F012008>.
30. M. P. Thake Jr, Effect of mistuning on bending-torsion flutter using a compressible time-domain aerodynamic theory, Master's thesis, The Ohio State University, Ohio, US, <http://hdl.handle.net/1811/38781> (2009).
31. Y. Leng, N. L. Key, Effects of nonuniform blade spacing on compressor rotor forced response and aeroacoustics, *Journal of Propulsion and Power* (2020) 1–11, doi:<https://doi.org/10.2514/1.B37866>.
32. S. H. Cho, T. Kim, S. J. Song, A time-domain fluid-structure interaction analysis of fan blades, in: *Turbo Expo: Power for Land, Sea, and Air*, Vol. 43154, 2008, pp. 703–712, doi:<https://doi.org/10.1115/GT2008-50479>.
33. Y. Demiroglu, M. A. Yukselen, Prediction of wind tunnel wall effects using panel methods, in: *10th Ankara International Aerospace Conference*, AIAC-2019, no. 136, Ankara Turkey, 2019, p. None, aiac.ae.metu.edu.tr/paper.php?No=AIAC-2019-136.
34. T. Wang, F. N. Coton, Numerical simulation of wind tunnel wall effects on wind turbine flows, *Wind Energy: An International Journal for Progress and Applications in Wind Power Conversion Technology* 3 (3) (2000) 135–148, doi:<https://doi.org/10.1002/we.35>.
35. D. L. Ashby, D. Sandlin, Application of a low order panel method to complex three-dimensional internal flow problems, Tech. rep., NASA Contractor report 177424, <https://ntrs.nasa.gov/citations/19860021529> (1986).
36. J. M. Verdon, Review of unsteady aerodynamic methods for turbomachinery aeroelastic and aeroacoustic applications, *AIAA journal* 31 (2) (1993) 235–250, doi:<https://doi.org/10.2514/3.11660>.
37. C. S. Prasad, L. Peek, Analysis of classical flutter in steam turbine blades using reduced order aeroelastic model, in: *The 14th International Conference on Vibration Engineering and Technology of Machinery (VETOMAC XIV)*, Lisbon, Portugal, 2018, pp. 150–156, doi:<https://doi.org/10.1051/mateconf/201821115001>.
38. P. Petrie-Repar, V. Makhnov, N. Shabrov, E. Smirnov, S. Galaev, K. Eliseev, Advanced flutter analysis of a long shrouded steam turbine blade, in: *Turbo Expo: Power for Land, Sea, and Air*, Vol. 45776, American Society of Mechanical Engineers, 2014, p. V07BT35A022, doi:<https://doi.org/10.1115/GT2014-26874>.
39. Dynamics of mistuned bladed-disk assemblies, accessed: 2020-09-14.
40. C. Meinzer, Numerical investigation of multi-row flutter interaction with wake excitation, Master's thesis, Department of Mechanical Engineering and Materials Science, Duke University) (2011).
41. E. F. Crawley, Aeroelastic formulation for tuned and mistuned rotors, Tech. rep., AGARD Manual on Aeroelasticity in Axial-Flow Turbomachines, Vol. 2, Structural Dynamics and Aeroelasticity, Chapter 19, AGARD-AG-298, <https://apps.dtic.mil/sti/citations/ADA199697> (1988).
42. A. Meldahl, Selbsterregte flügel-schwingungen mit einem freiheitsgrad, *Brown Boveri Mitteilungen* 12 (1946) 386–393.
43. S. P. Fiddes, J. H. Gaydon, A hybrid panel/image method for calculating wall constraint effects in subsonic wind tunnels., in: *Congress of the International Council of the Aeronautical Sciences*, Vol. 19, ICAS, 1994, pp. 740–750, https://www.icas.org/ICAS_ARCHIVE/ICAS1994/ICAS-94-3.3.2.pdf.
44. Y. C. Fung, *An Introduction to the Theory of Aeroelasticity*, 7th Edition, Dover Publication

- Inc, Mineola, New York, 2008, <https://store.doverpublications.com/0486469360.html>.
- 1165 45. V. Slama, B. Rudas, J. Ira, A. Macalka, P. Eret, V. Tsymbalyuk, Experimental and cfd investigation of aerodynamic forces and moments in a linear turbine blade cascade, in: ASME International Mechanical Engineering Congress and Exposition, Vol. 52033, American Society of Mechanical Engineers, 2018, p. V04AT06A041, doi:<https://doi.org/10.1115/IMECE2018-86667>.
- 1170
46. I. K. Hanna, Aerodynamic measurements on stationary and vibrating turbine blade cascade, Master's thesis, <https://dspace5.zcu.cz/handle/11025/38779> (2019).
- 1175
47. J. Ezquerro, Panel method for the aerodynamic calculation of mixed configurations with finite thickness and zero thickness, Ph.D. thesis, Universidad Politécnica de Madrid, http://oa.upm.es/47390/1/JOSE_MIGUEL_EZQUERRO_NAVARRO.pdf (2017).
- 1180
48. S. Yon, J. Katz, A. Plotkin, Effect of airfoil (trailing-edge) thickness on the numerical solution of panel methods based on the dirichlet boundary condition, AIAA journal 30 (3) (1992) 697–702, doi:<https://doi.org/10.2514/3.10974>.
- 1185
49. D. M. Vogt, T. H. Fransson, Experimental investigation of mode shape sensitivity of an oscillating low-pressure turbine cascade at design and off-design conditions, Journal of engineering for gas turbines and power 129 (2) (2007) 530–541, doi:<https://doi.org/10.1115/1.2436567>.
- 1190
50. E. Camara, Validation of time domain flutter prediction tool with experimental results, Ph.D. thesis, Kungliga Tekniska Hogskolan(KTH), Stockholm, Sweden, <https://www.diva-portal.org/smash/record.jsf?pid=diva2%3A790267&dswid=-1674> (2015).
- 1195
51. C. S. Prasad, L. Pesek, Classical flutter study in turbomachinery cascade using boundary element method for incompressible flows, in: T. Uhl (Ed.), Advances in Mechanism and Machine Science, Springer International Publishing, Cham, 2019, pp. 4055–4064, doi:https://doi.org/10.1007/978-3-030-20131-9_404.
- 1200
- 1205

Figures

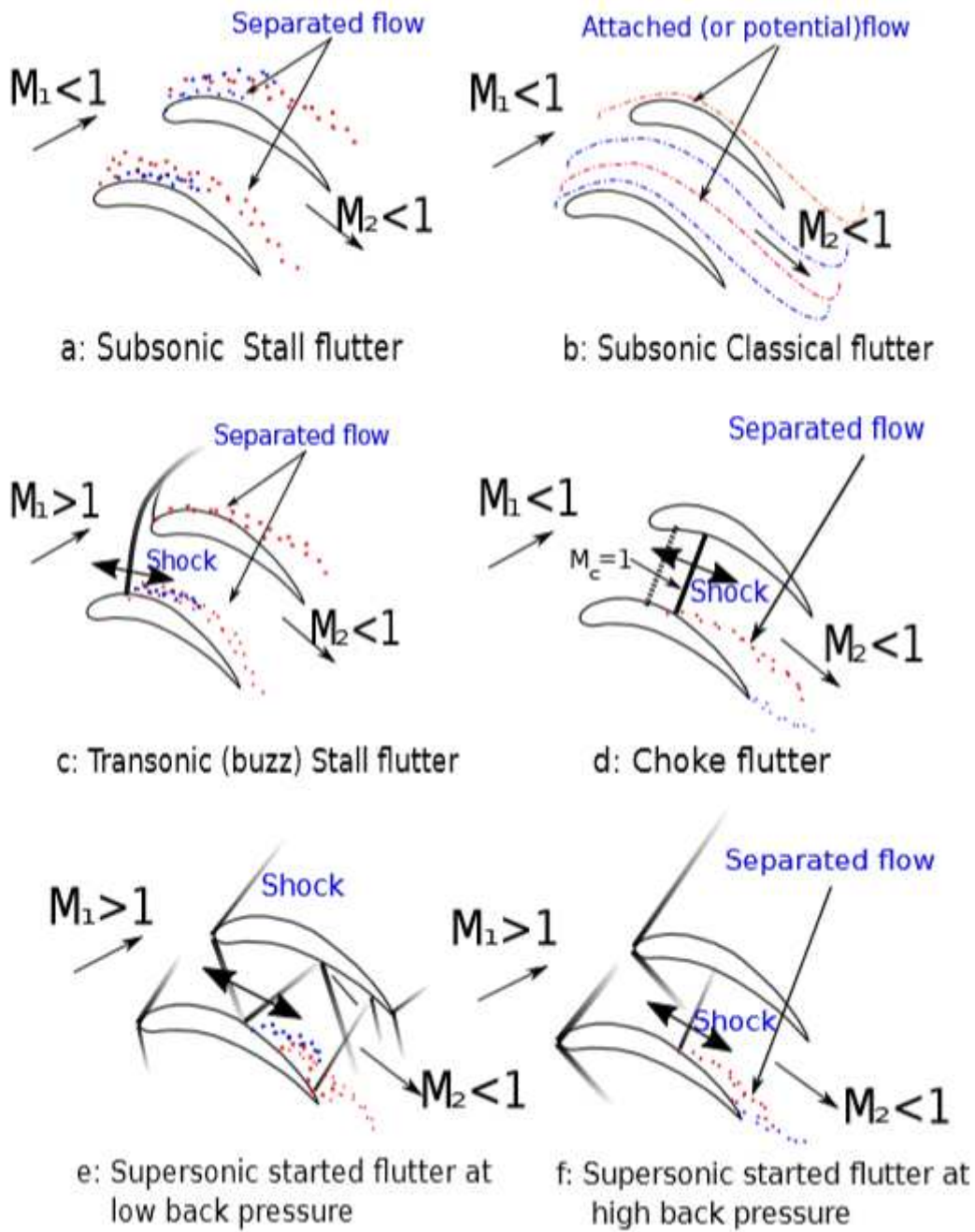


Figure 1

Flutter chart for in the turbomachinery

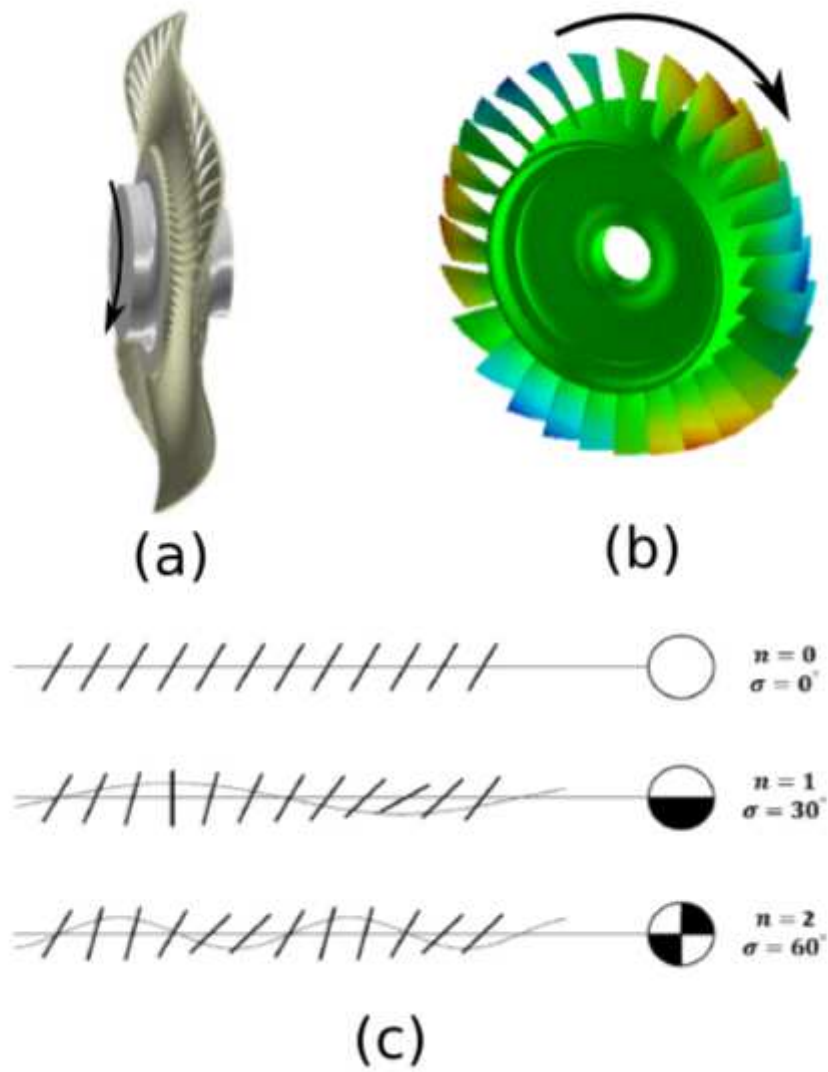
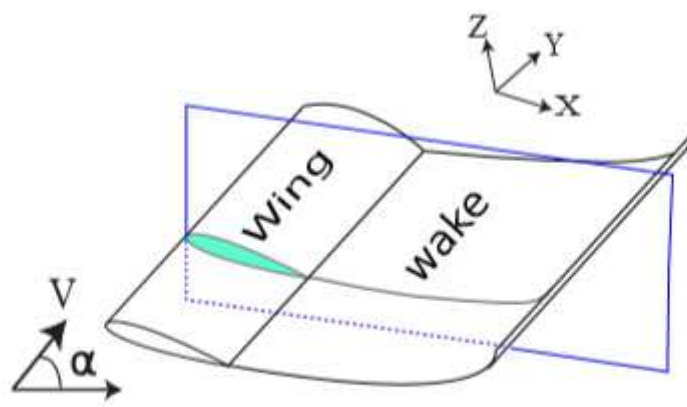
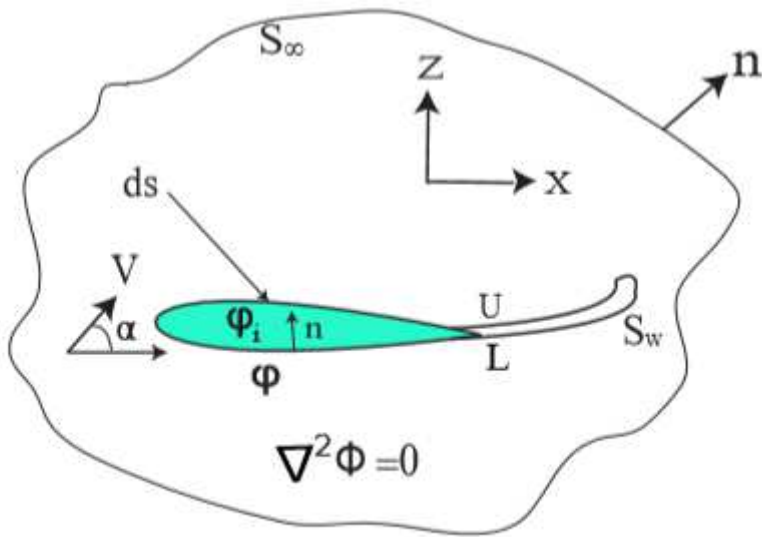


Figure 2

TWM oscillation and IBPA: (a) and (b) 3D representation of TW with 5 and 3 ND [38, 39] (c) 2D representation of TWM (ND=12);torsional flutter in linear cascade [40]



(a)



(b)

Figure 3

Cross section of wing with time dependent wake panels

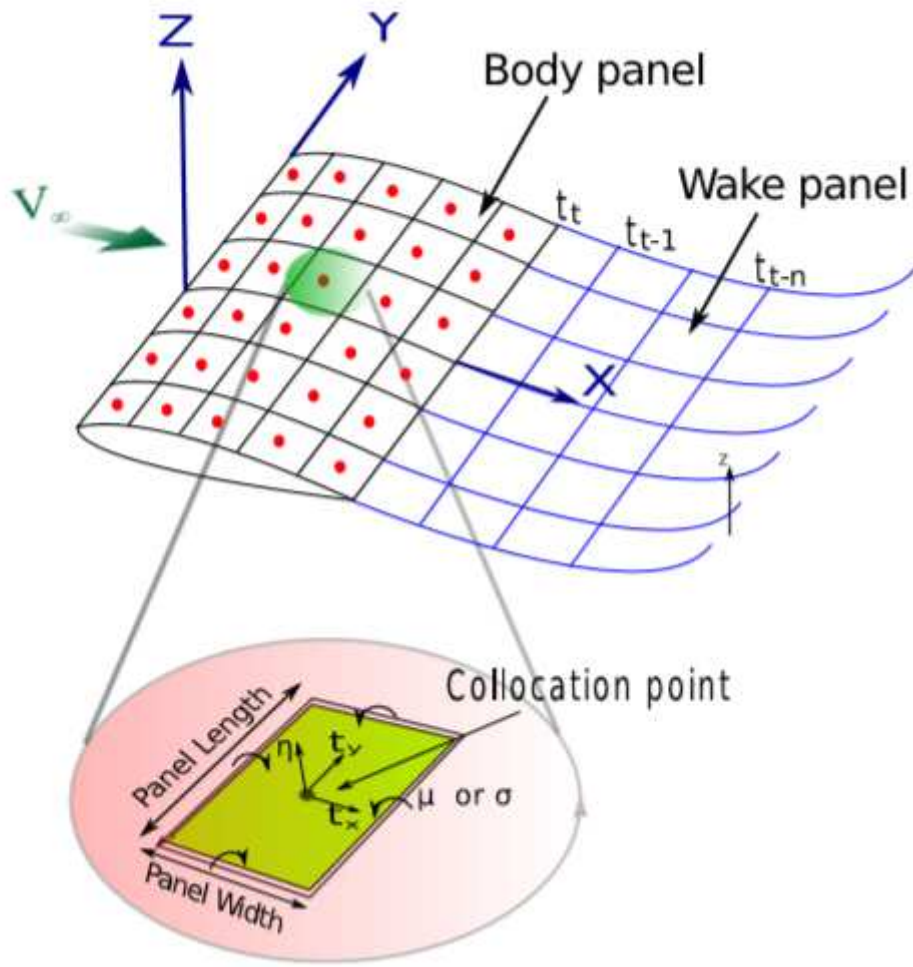


Figure 4

PM discretization of wing using source and doublet singularities elements

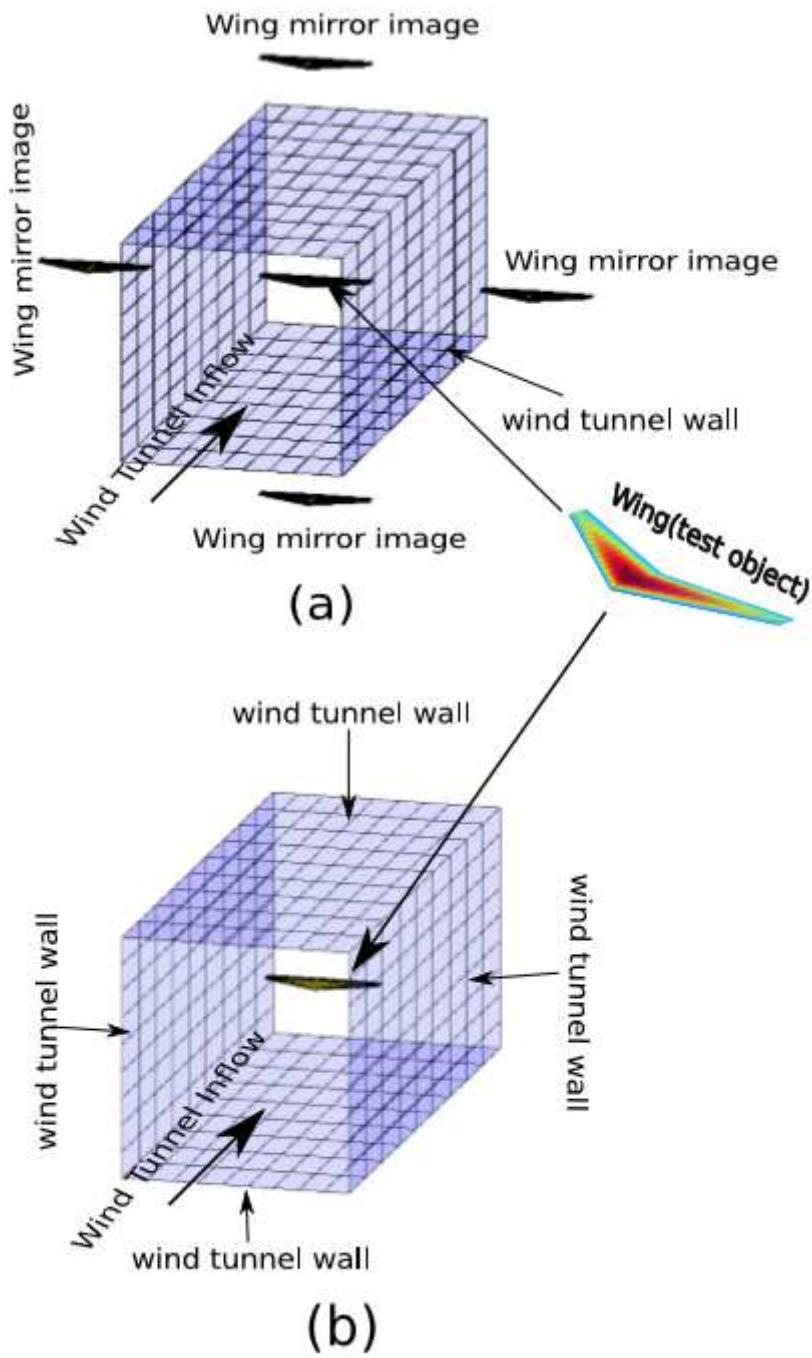


Figure 5

Different method to simulate wall effects using PM (a) mirror image method (b) direct wall (source elements) method.

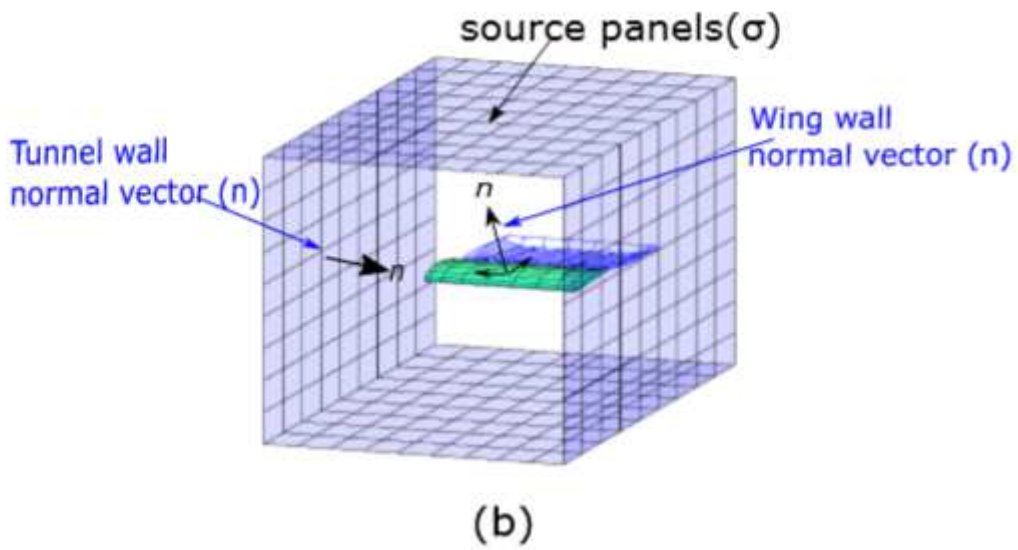
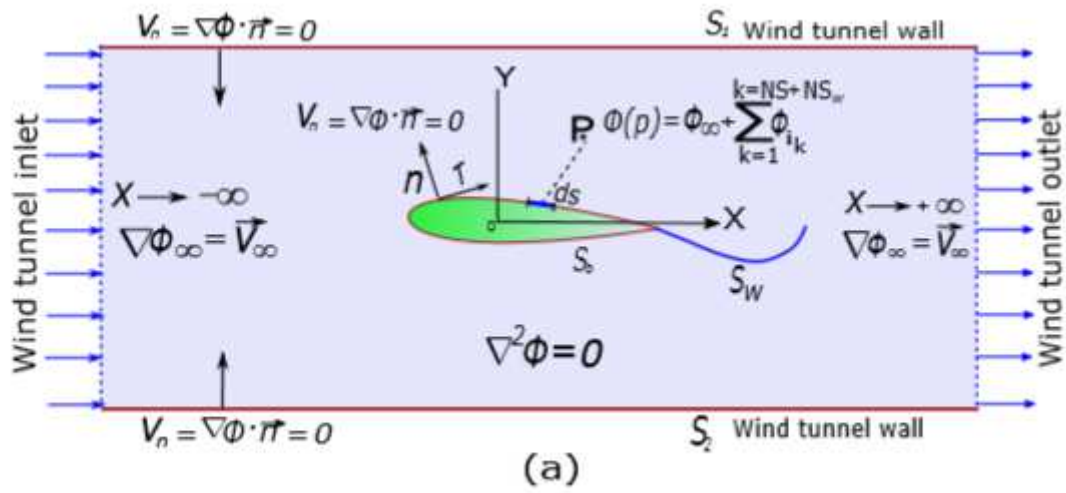


Figure 6

Direct wall method to simulate wall effect in internal flow PM application .

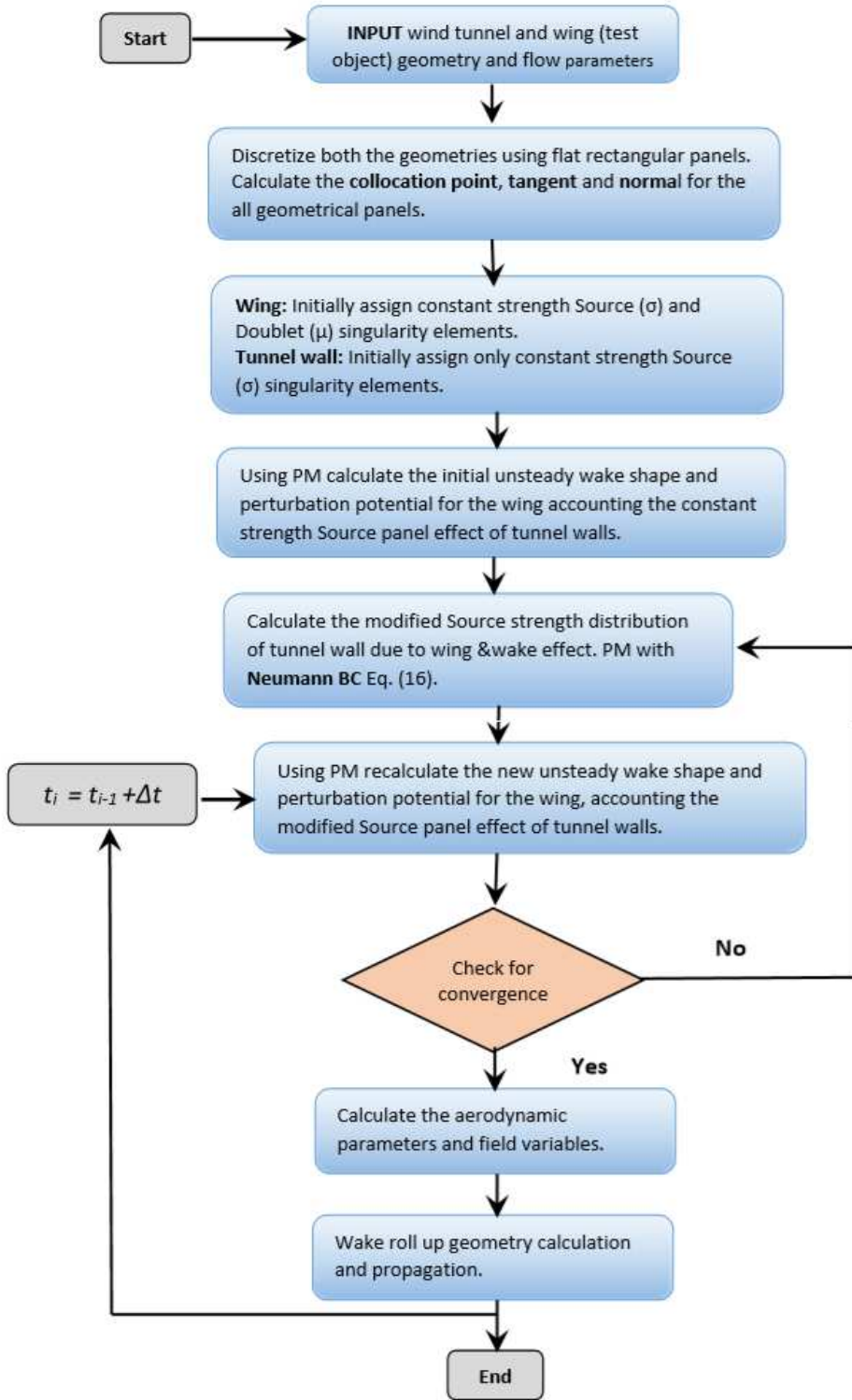


Figure 7

Flowchart algorithm for wind tunnel wall interference calculation in internal flow using PM

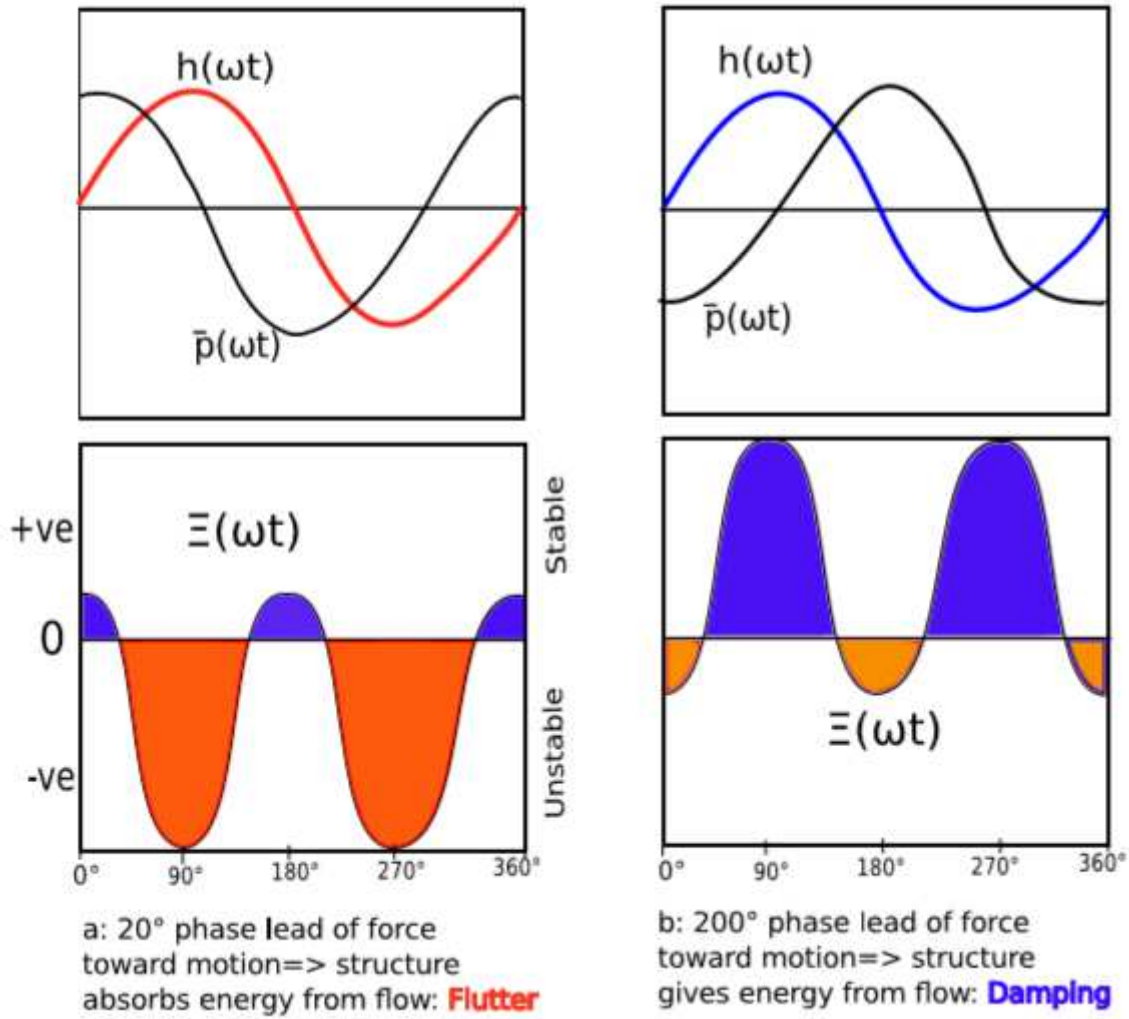


Figure 8

Schematic illustration of FSI. (a) Flutter: aeroelastically unstable (b) Damped vibration: aeroelastically stable

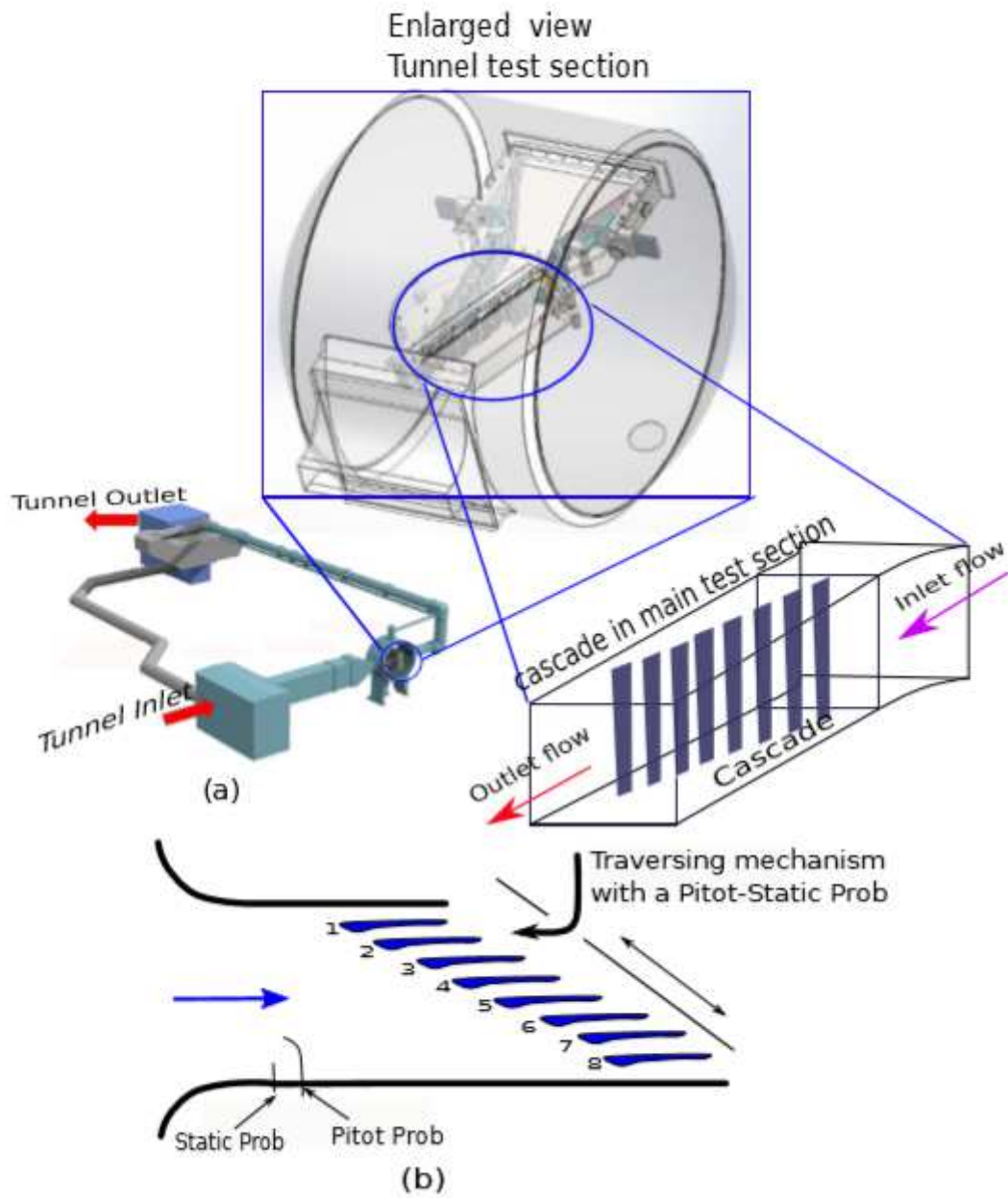


Figure 9

UWB linear cascade test setup (a) Test wind tunnel with test section (b) 2D view of the cascade geometry [45]

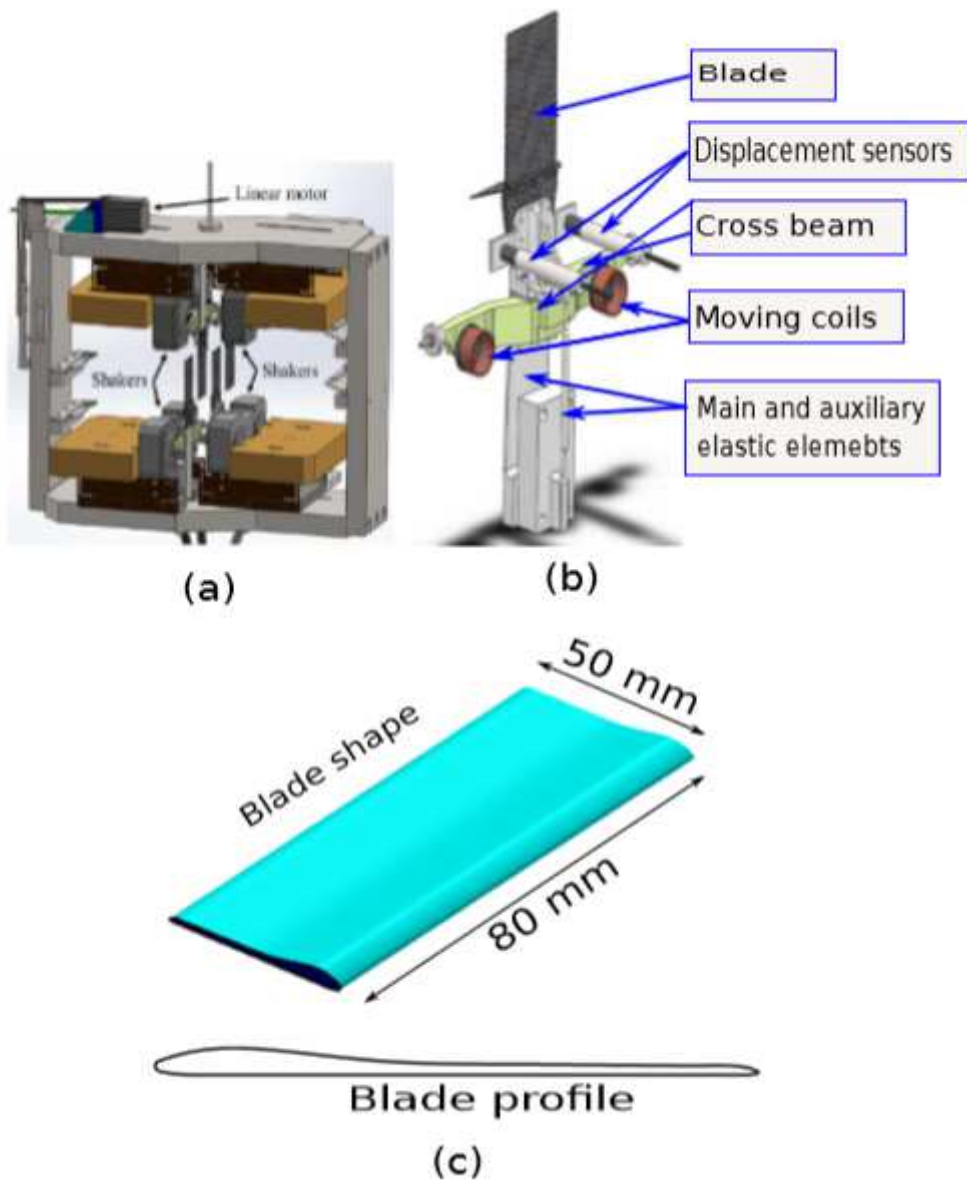


Figure 10

UWB linear cascade test setup (a) blade and shaker assembly (b) Elastic suspension (c) Blade geometry. [45]

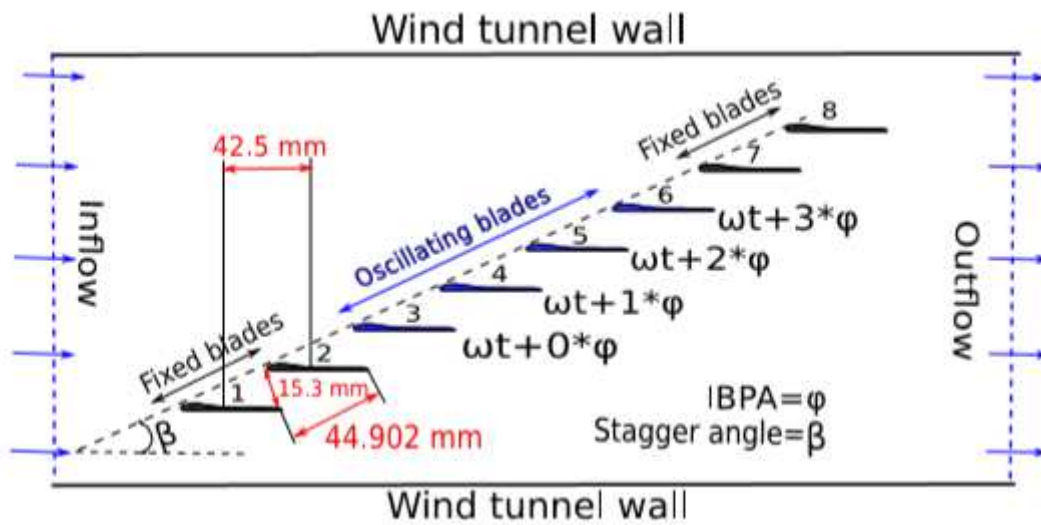


Figure 11

UWB linear cascade oscillating sequence in TWM mode

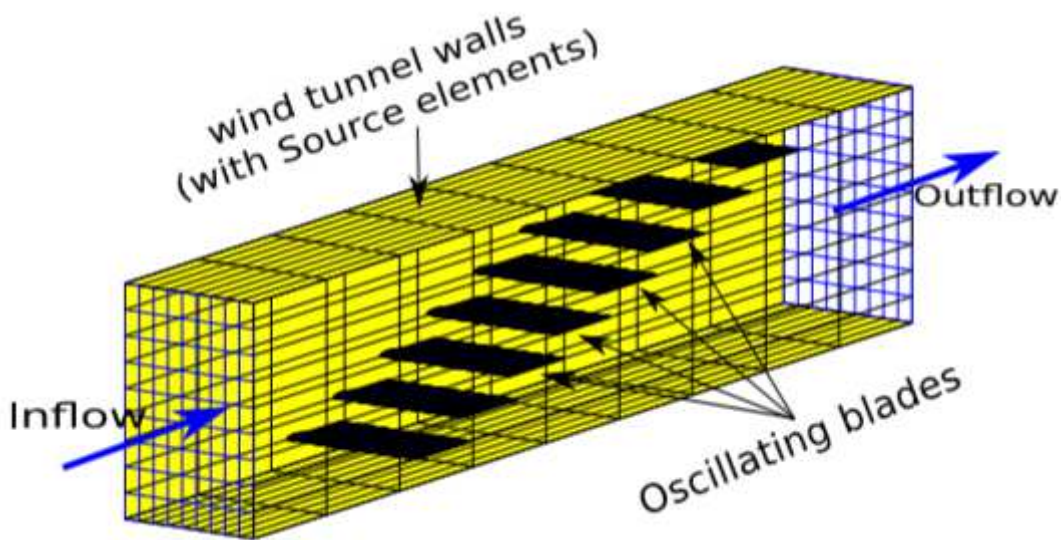


Figure 12

Grid strategy of direct wall method PM numerical model of UWB test cascade

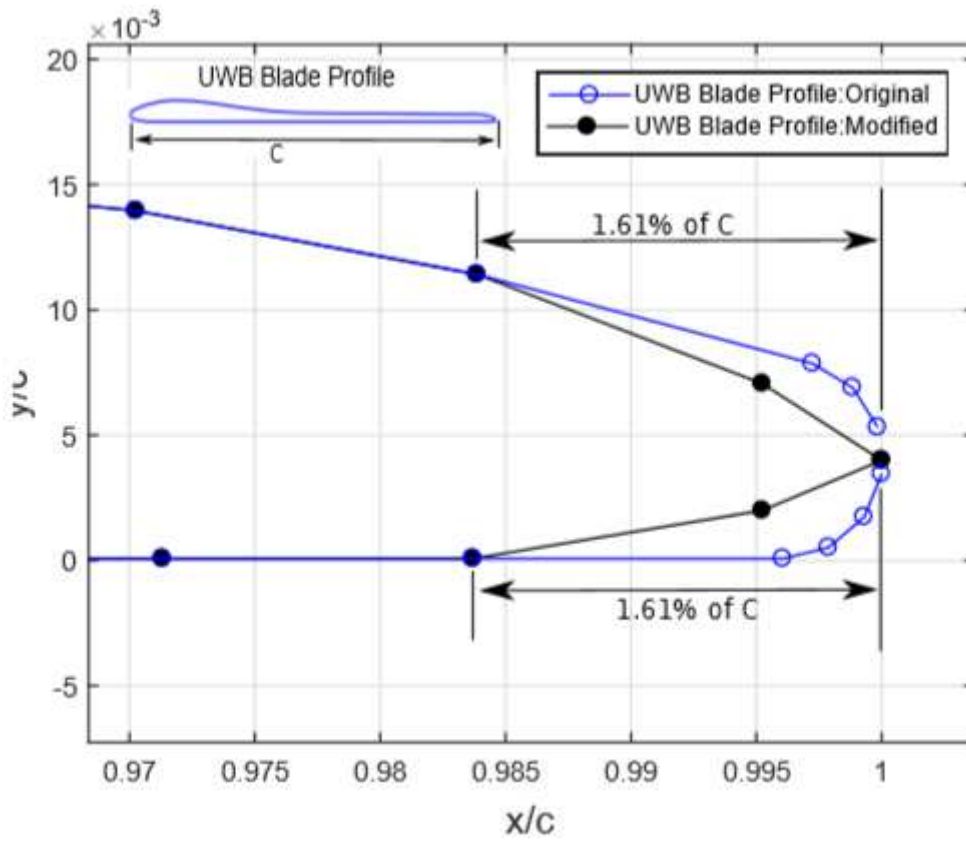


Figure 13

Modification of UWB blade's trailing edge profile for PM-ROAM

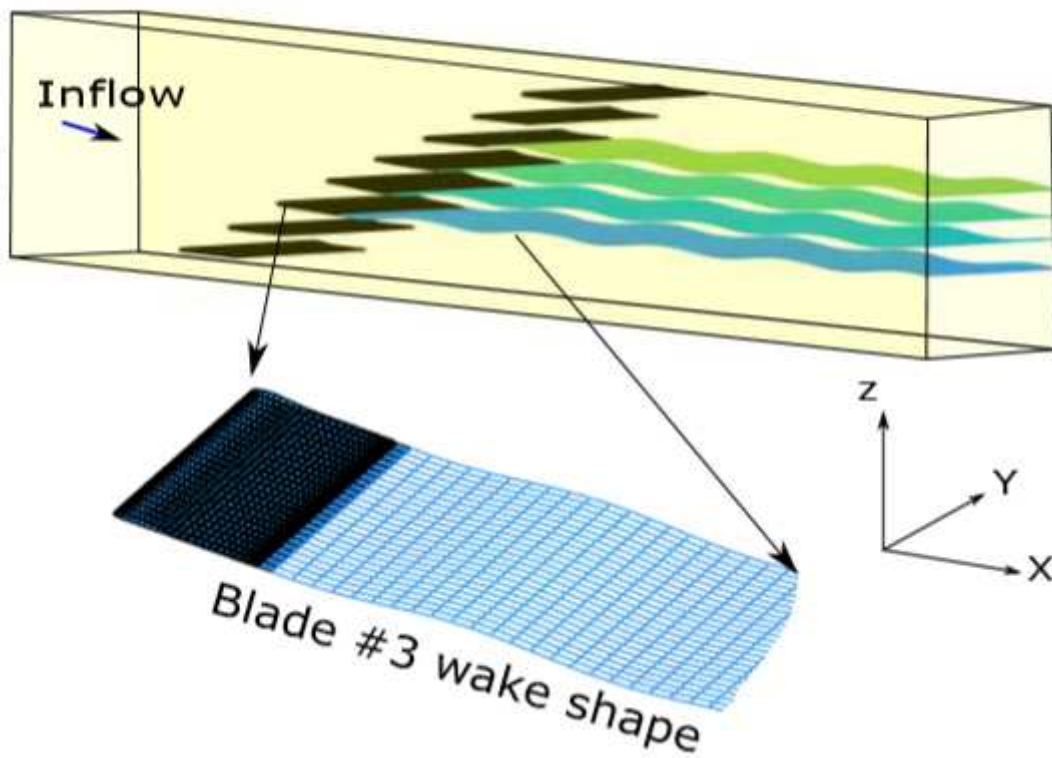
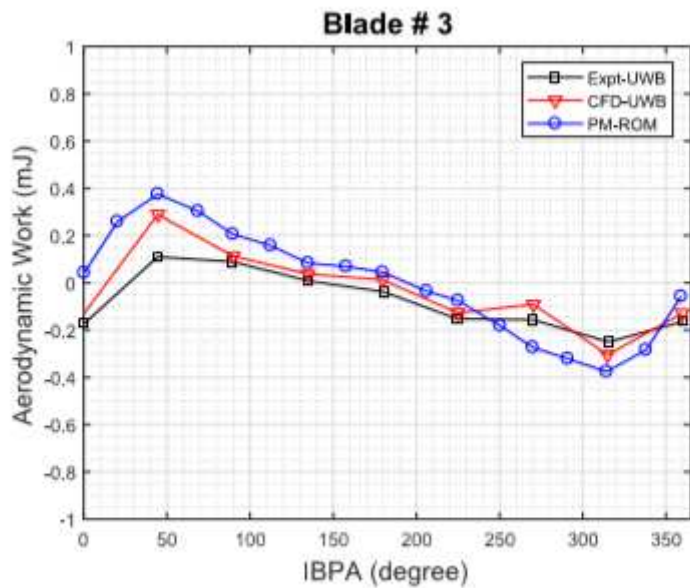
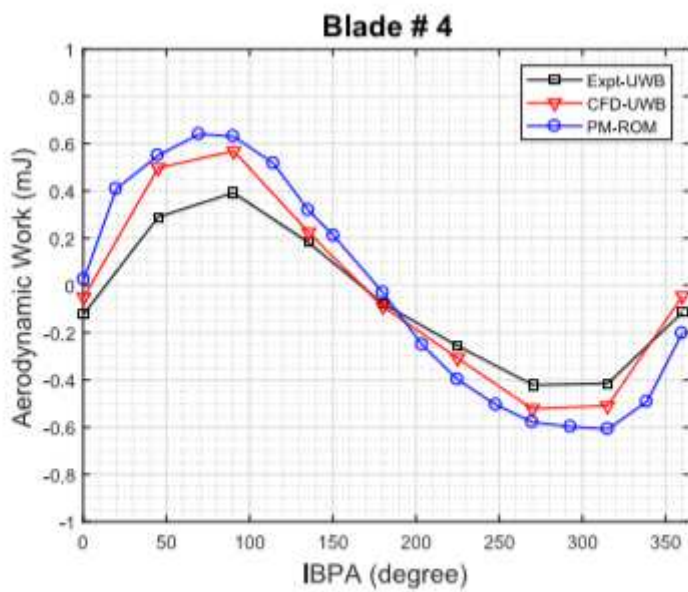


Figure 14

UWB cascade wake shape of oscillating blade #3



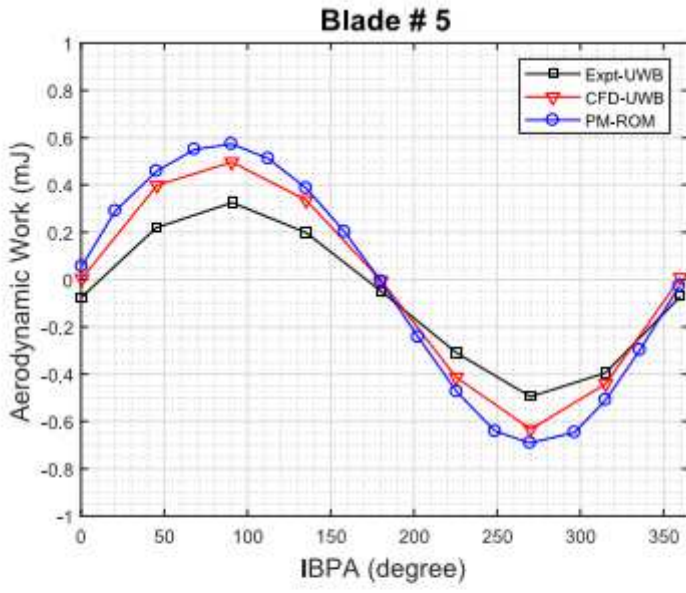
(a)



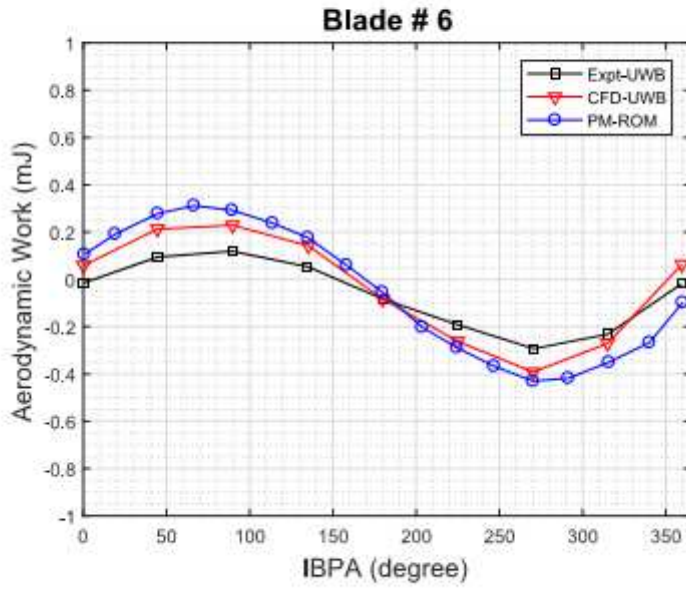
(b)

Figure 15

Comparisons of Aerodynamic work(mJ) vs IBPA ; PM-ROAM vs Experimental and CFD(CFX) (a)#3 (b) #4 : Torsional flutter



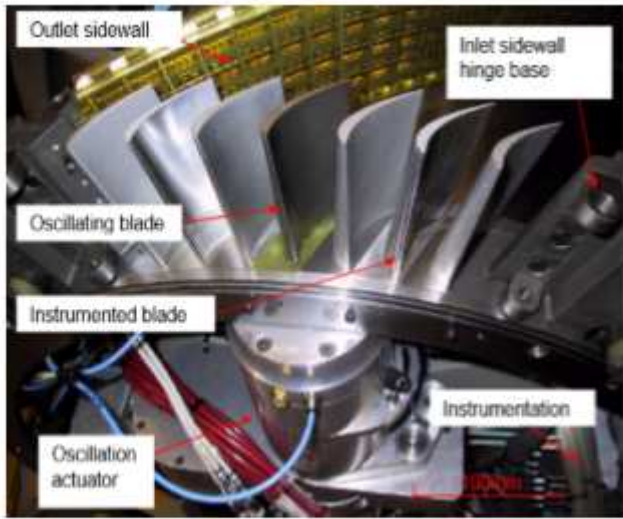
(c)



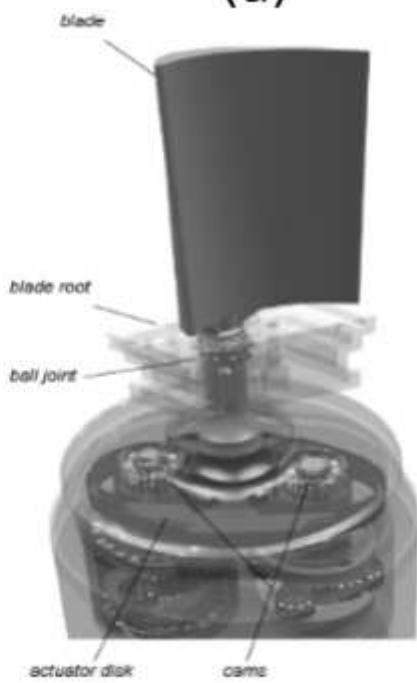
(d)

Figure 16

Comparisons of Aerodynamic work(mJ) vs IBPA ; PM-ROAM vs Experimental and CFD(CFX)(a)#5 (b) #6 : Torsional flutter



(a)



(b)

Figure 17

Experimental setup of KTH 3D blade cascade and oscillation mechanism [9]

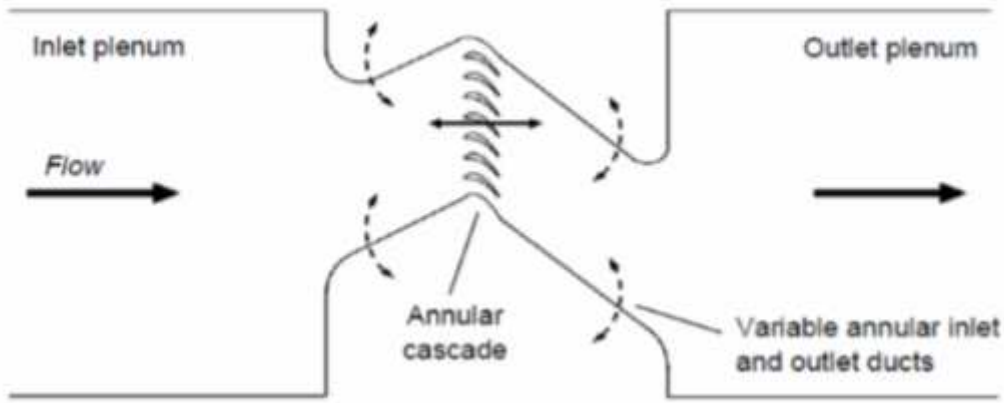


Figure 18

Schematic diagram of KTH cascade test setup [9]

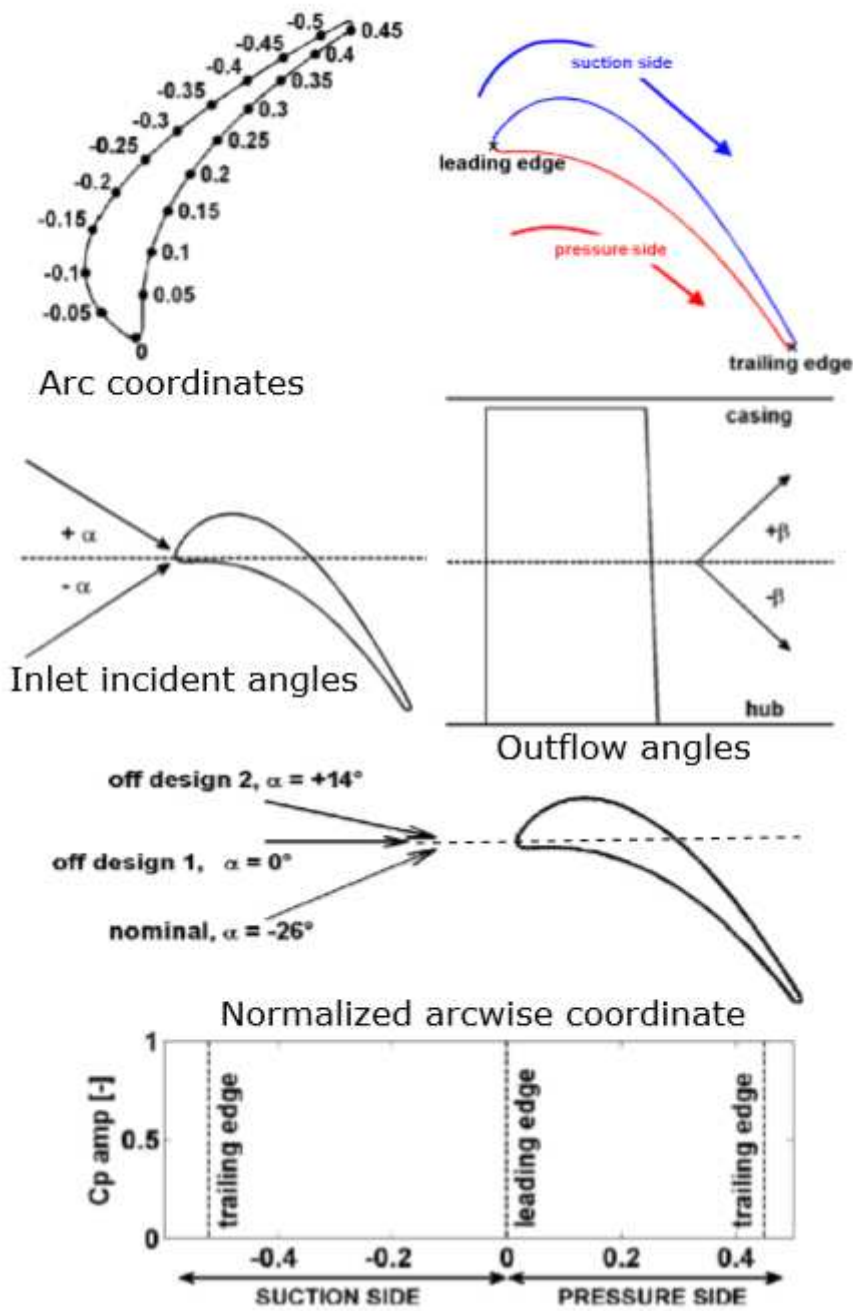


Figure 19

KTH cascade coordinate conventions [9]

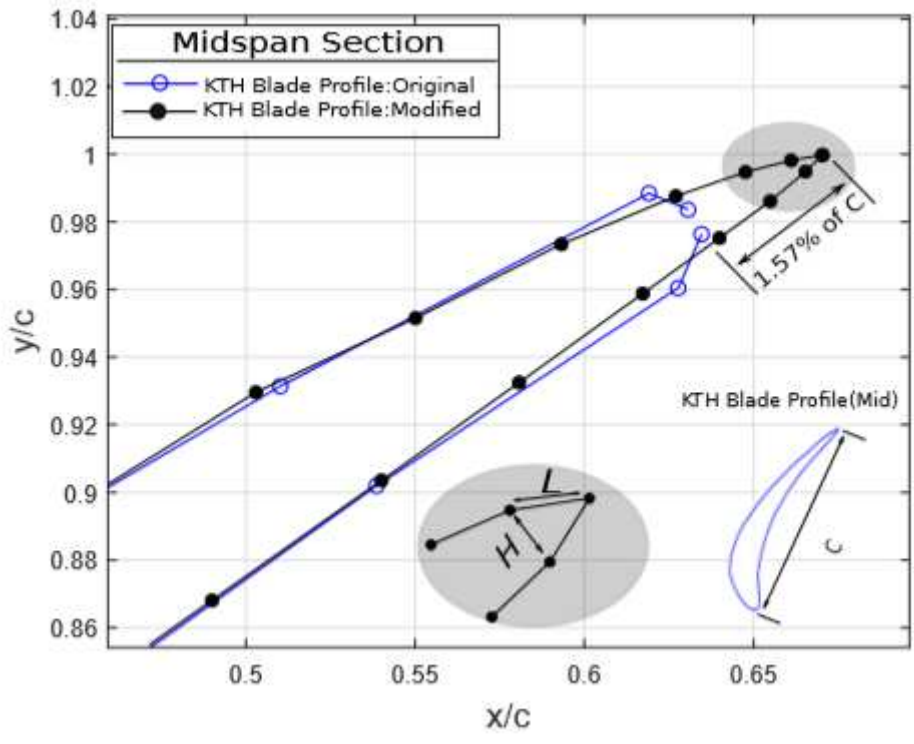


Figure 20

Modification of KTH blade's trailing edge profile for ROAM-PM and Thickness-ratio (H/L)

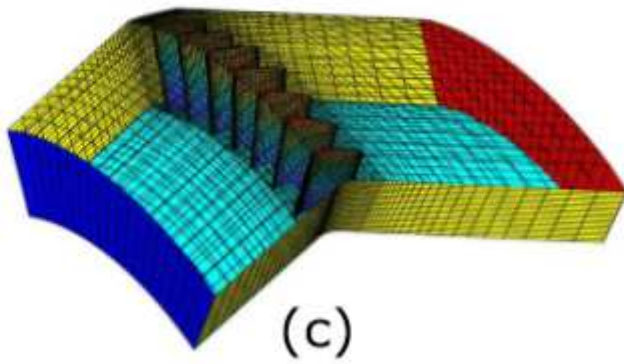
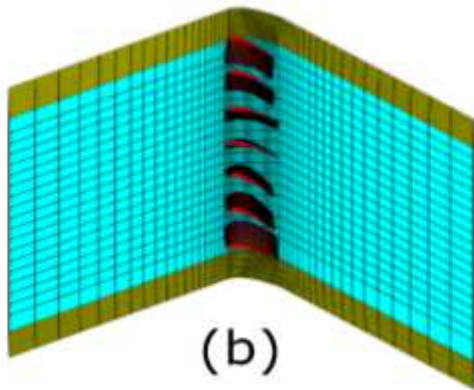
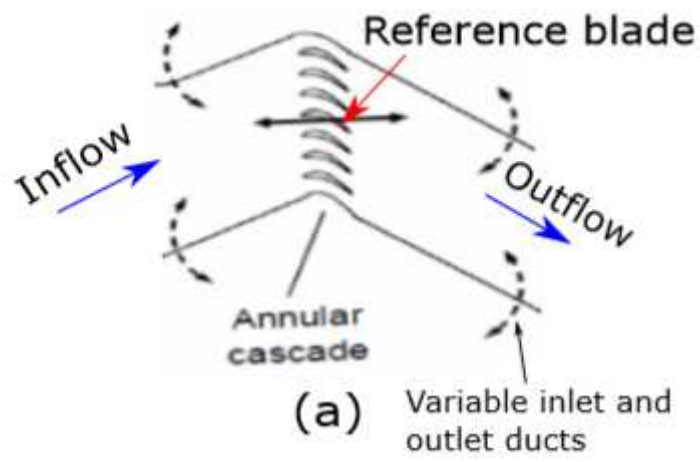


Figure 21

PM numerical model of KTH tunnel and cascade

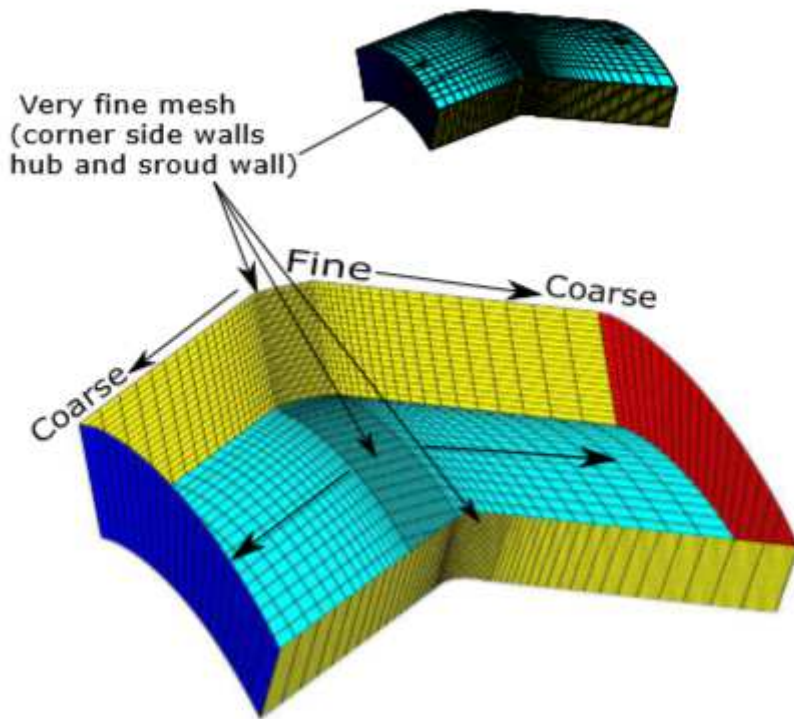


Figure 22

Mesh strategy for PM numerical model of KTH tunnel and cascade

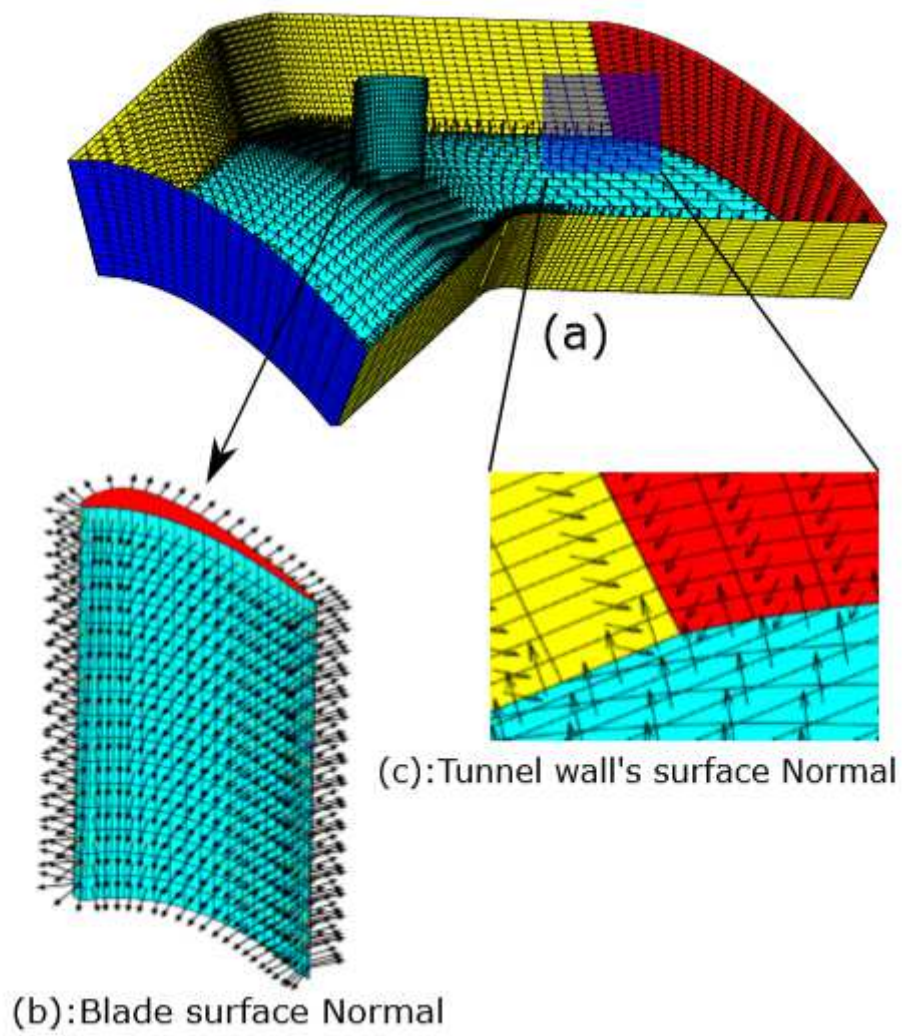


Figure 23

Wind tunnel wall and reference blade normal (n)

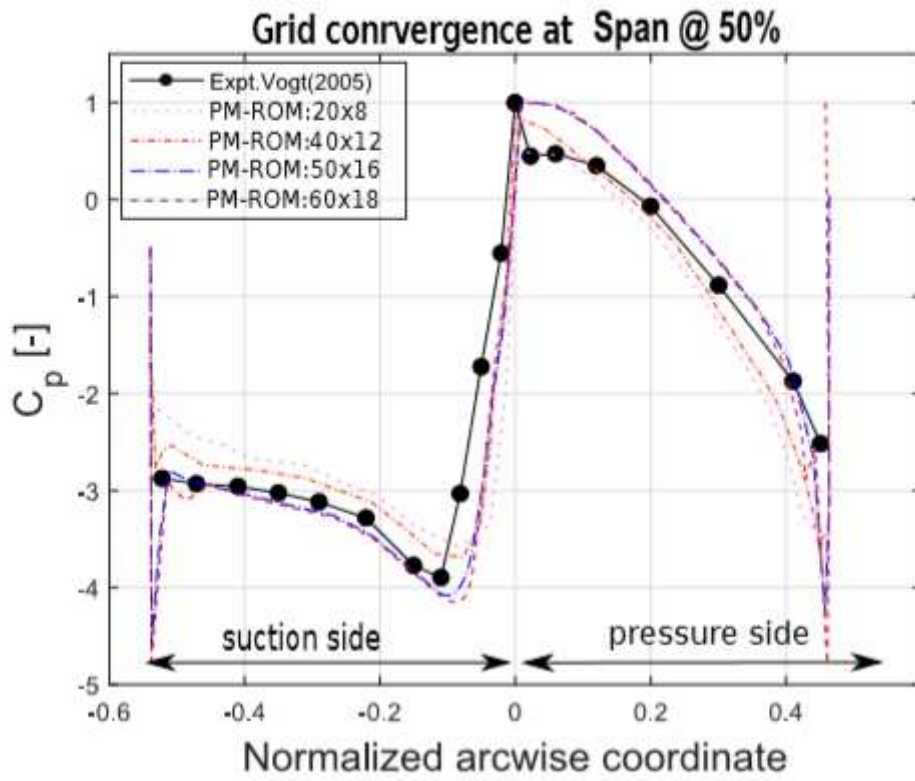


Figure 24

Grid convergence study of KTH cascade for different value chord wise and panel wise panel numbers.

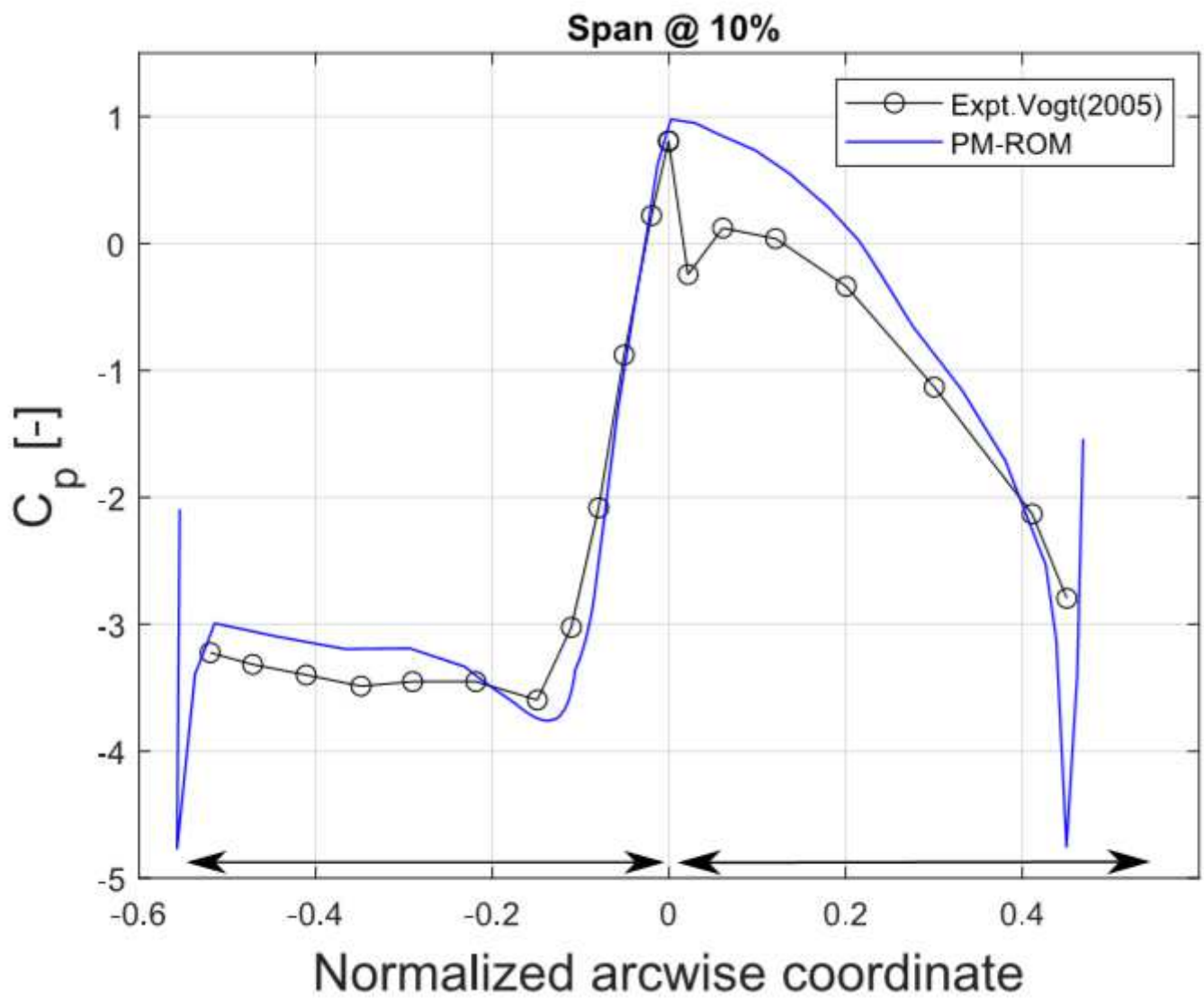


Figure 25

Steady C_p distribution at 10% spanwise position; low subsonic, nominal inflow OP

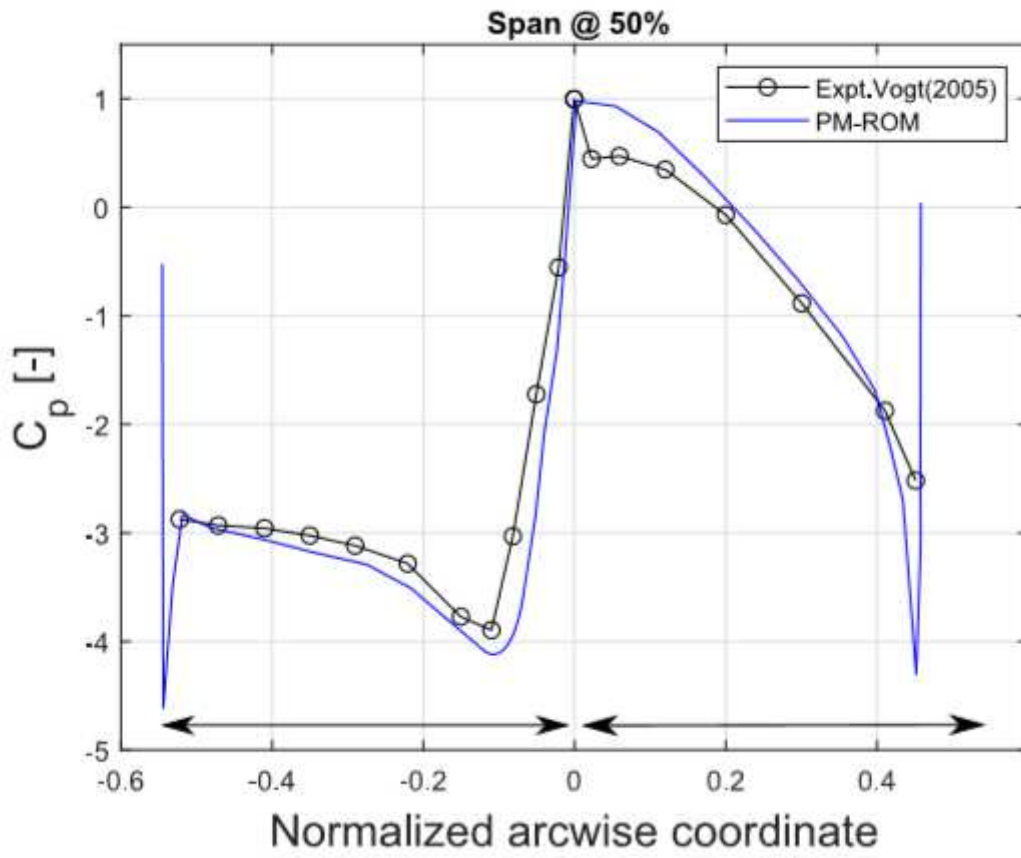


Figure 26

Steady C_p distribution at 50% spanwise position; low subsonic, nominal inflow OP

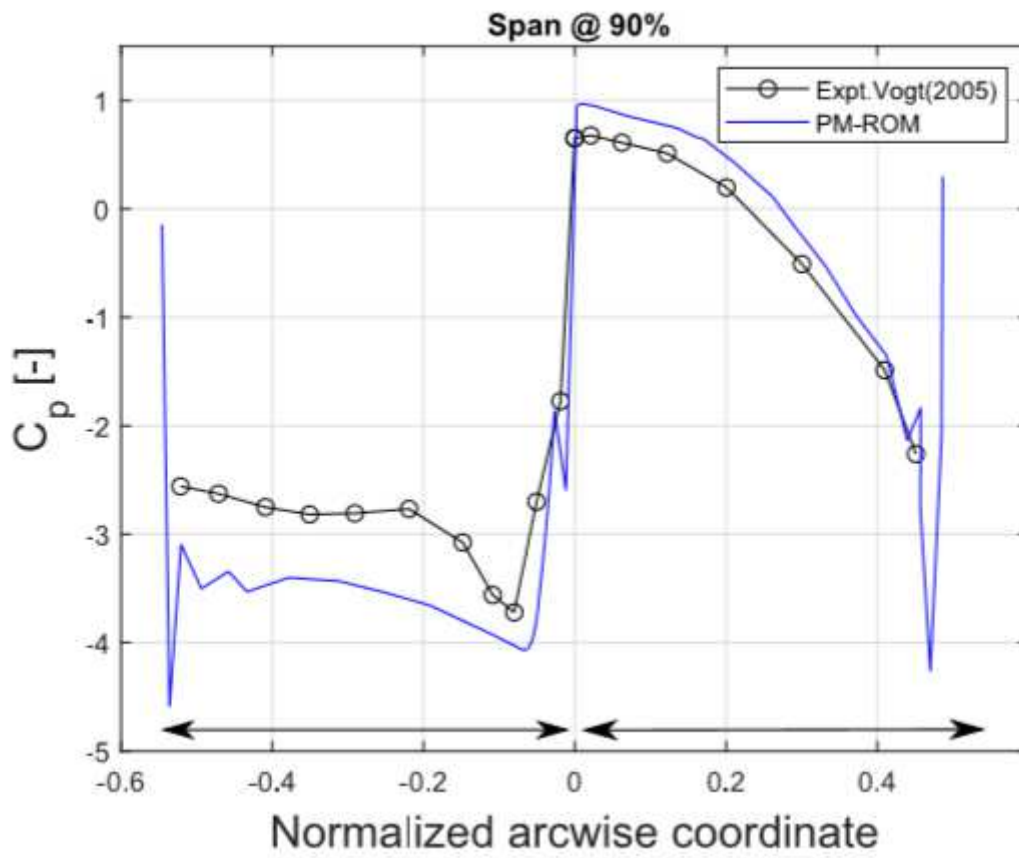


Figure 27

Steady C_p distribution at 90% spanwise position; low subsonic, nominal inflow OP

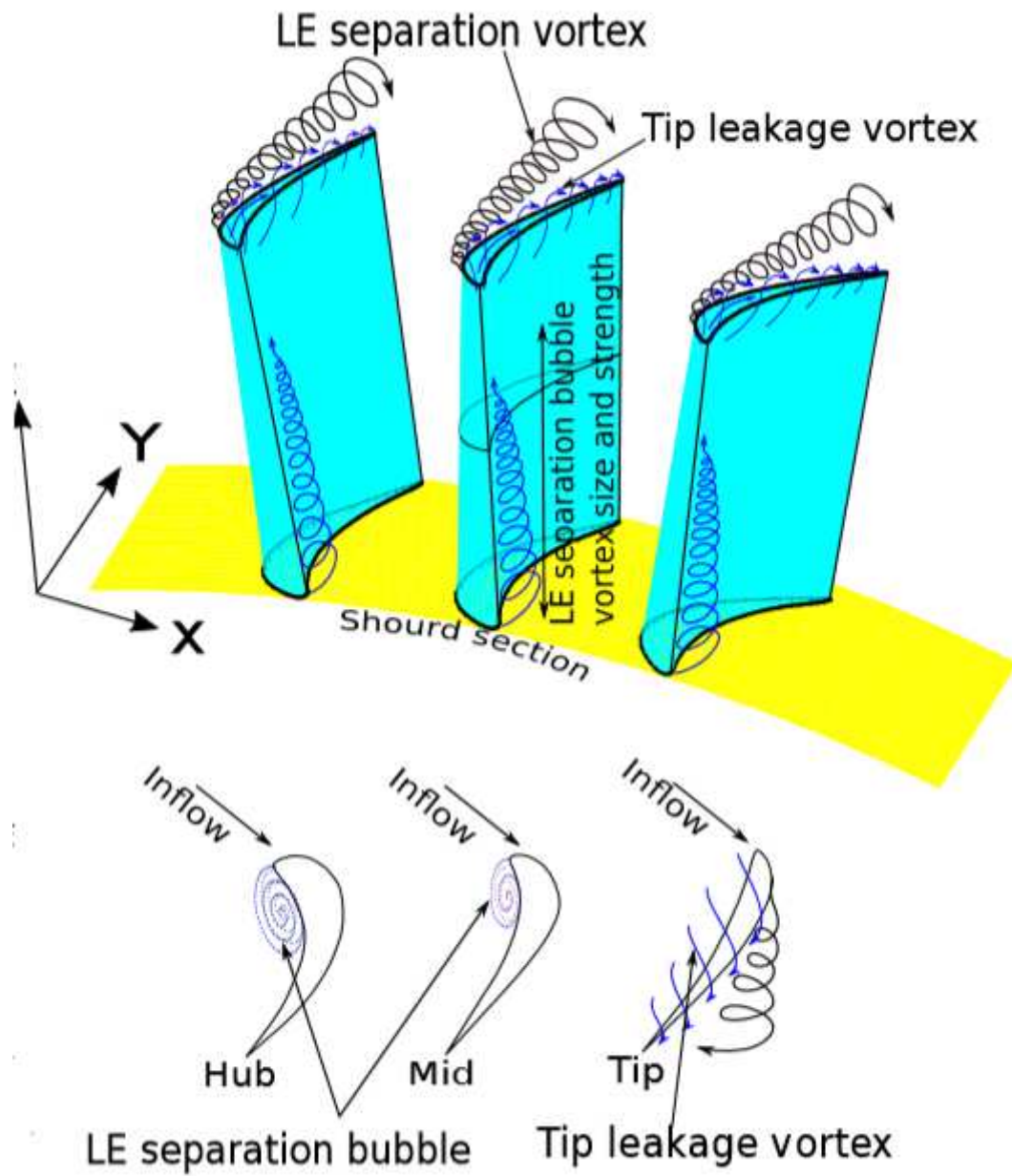


Figure 28

Schematic representation of axial vortex and tip leakage in 3D blade cascade

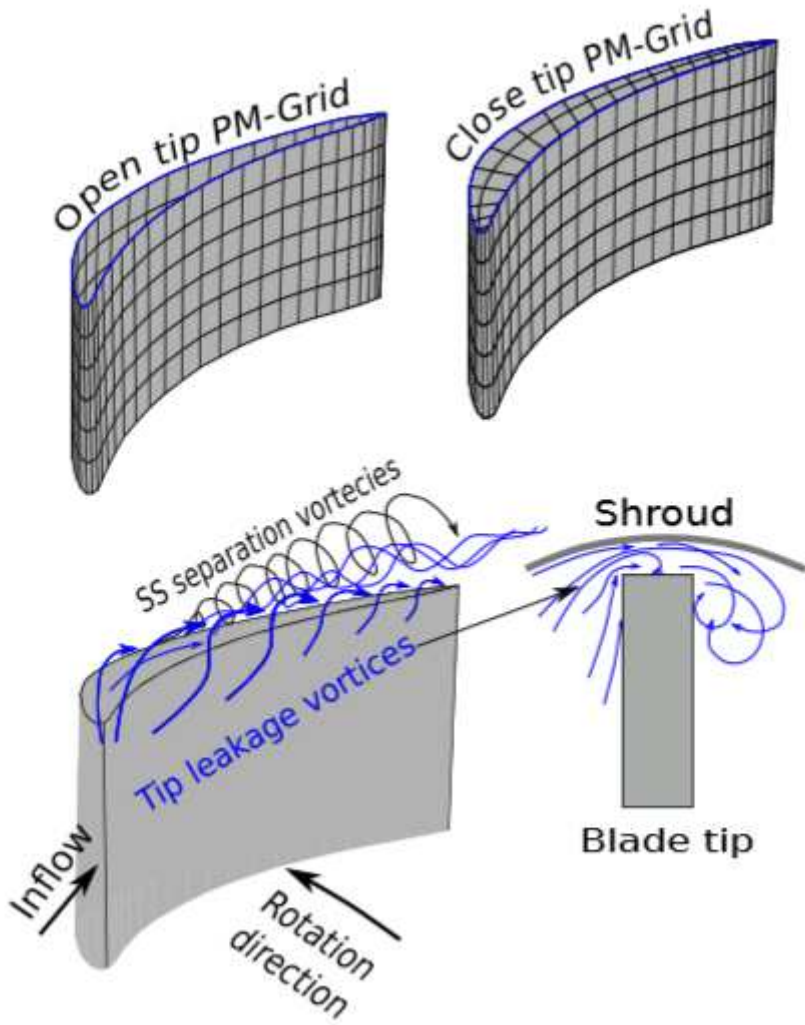


Figure 29

Schematic representation of tip clearance, tip shapes and tip leakage in 3D blade cascade

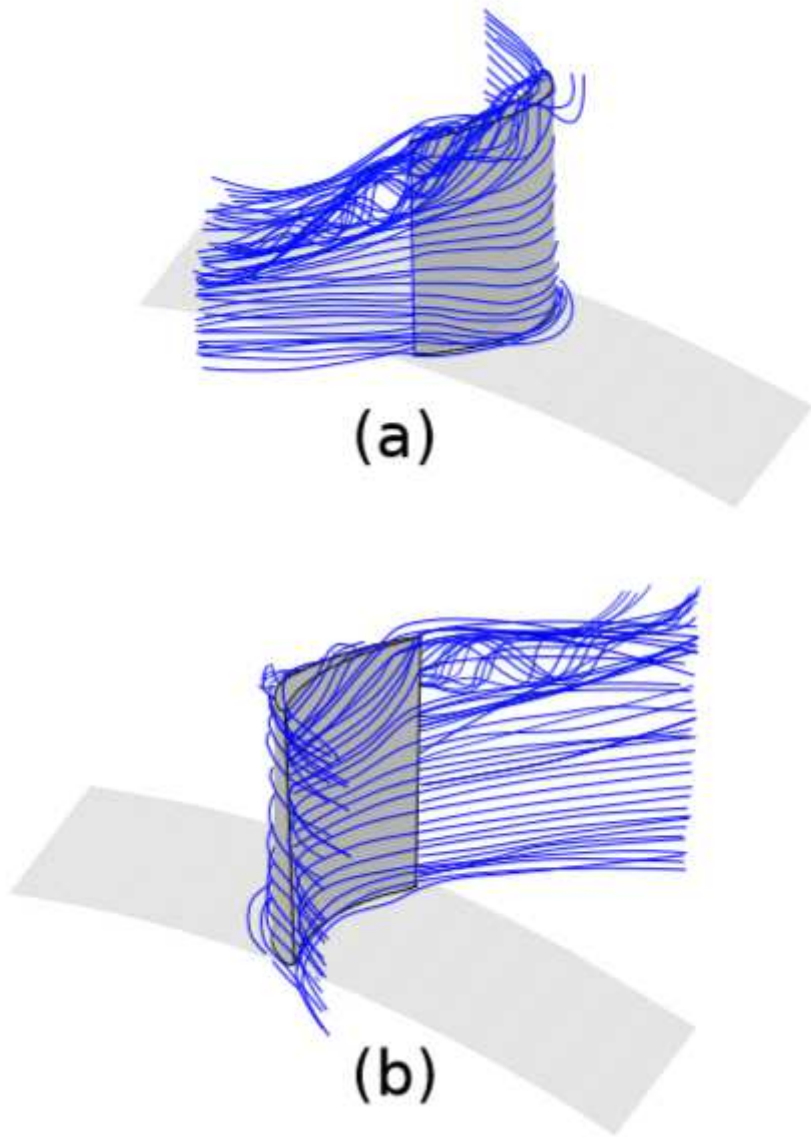


Figure 30

Schematic representation of tip clearance, tip shapes and tip leakage in 3D blade cascade

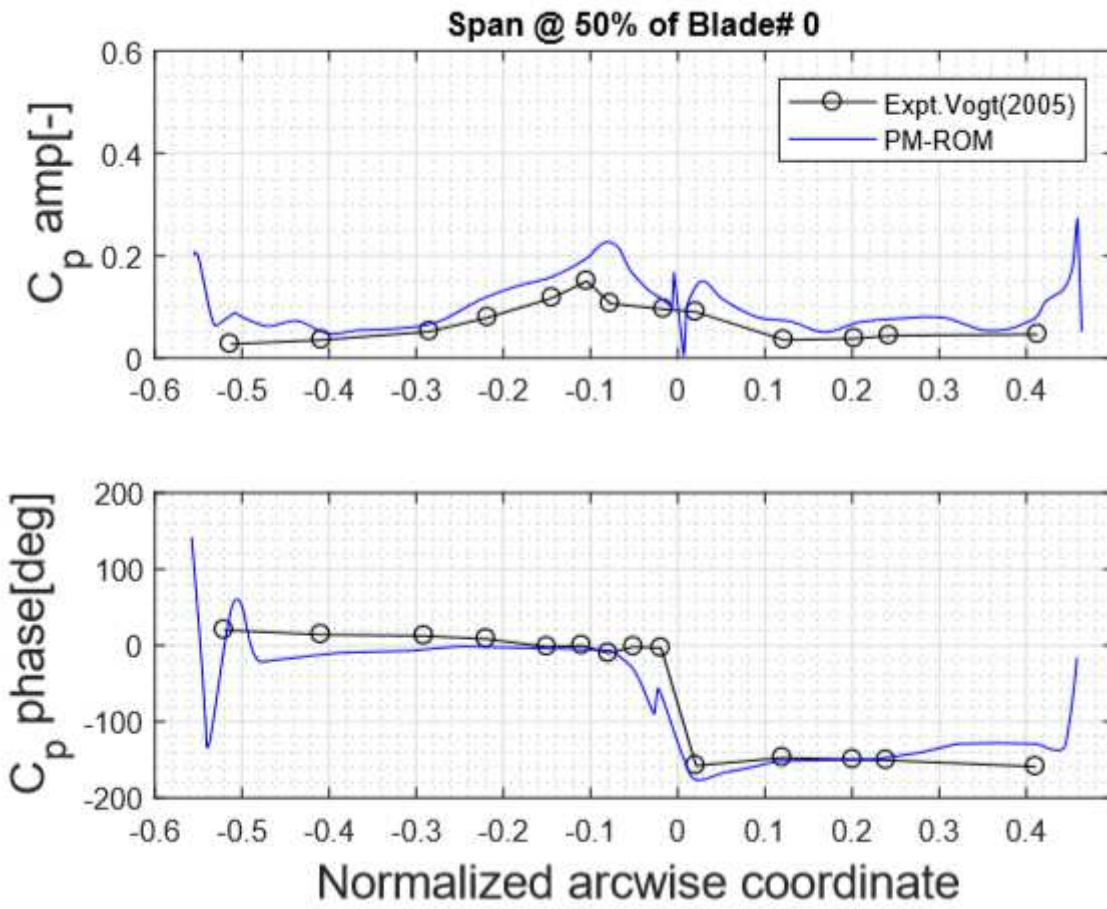


Figure 31

Comparison of measured and predicted unsteady response on blade#0 at mid span for torsional mode flutter; low subsonic, nominal inflow OP, $k=0.1$

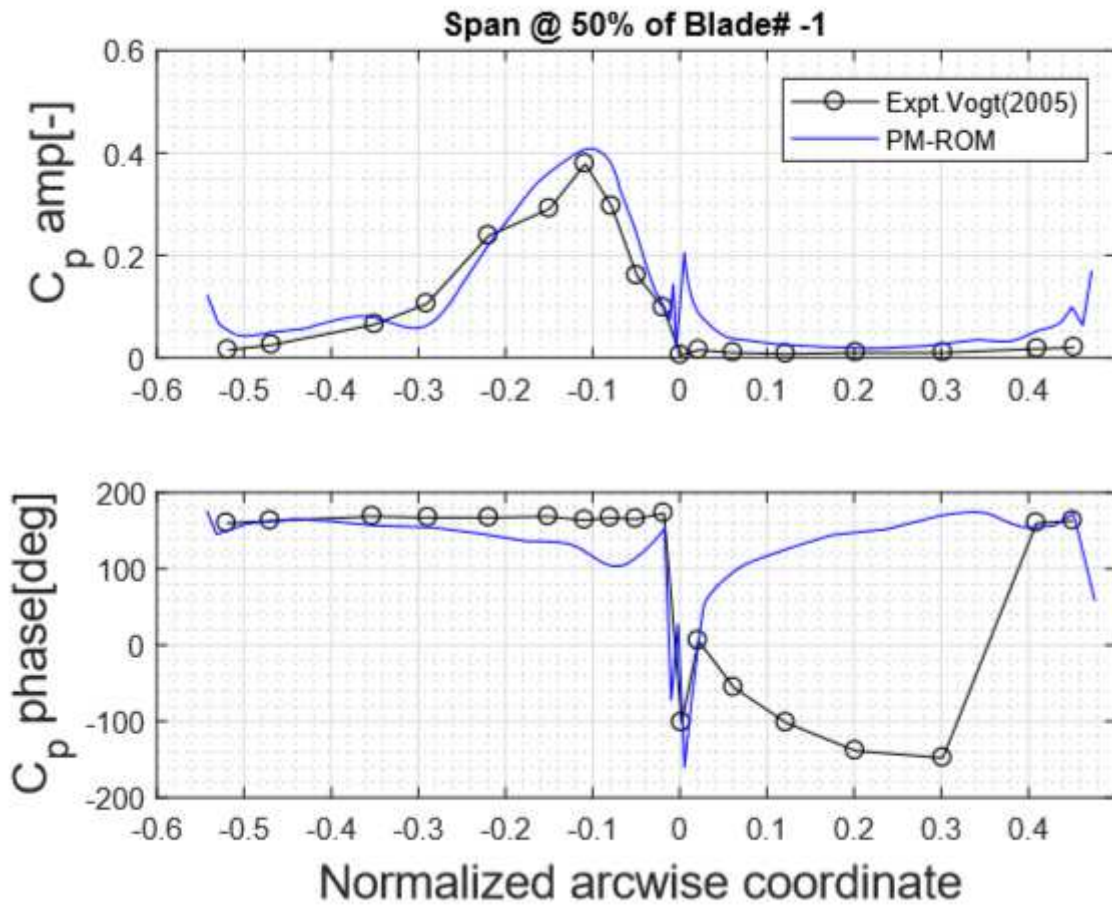


Figure 32

Comparison of measured and predicted unsteady response on blade -1 at mid span for torsional mode flutter; low subsonic, nominal inflow OP, $k=0.1$

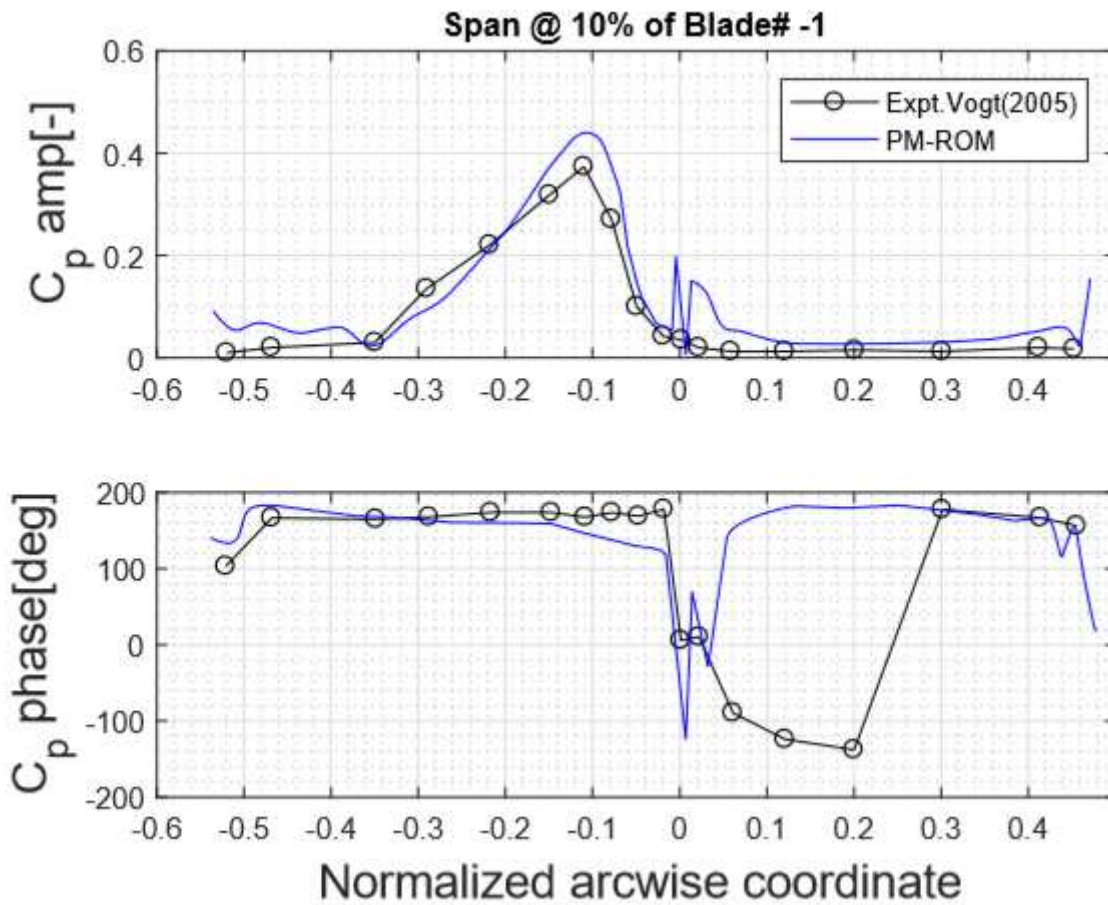


Figure 33

Comparison of measured and predicted unsteady response on blade# -1 at 10% span for torsional mode flutter; low subsonic, nominal inflow OP , $k=0.1$

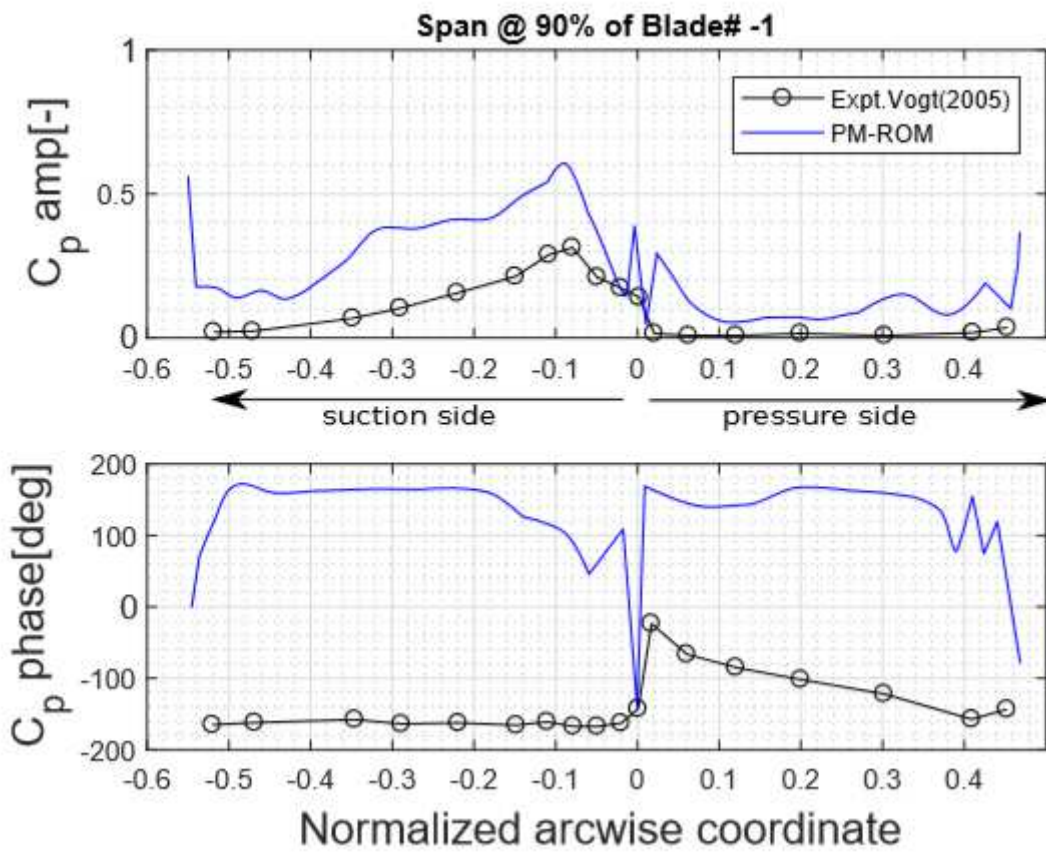


Figure 34

Comparison of measured and predicted unsteady response on blade -1 at 90% span for torsional mode flutter; low subsonic, nominal inflow OP , $k=0.1$

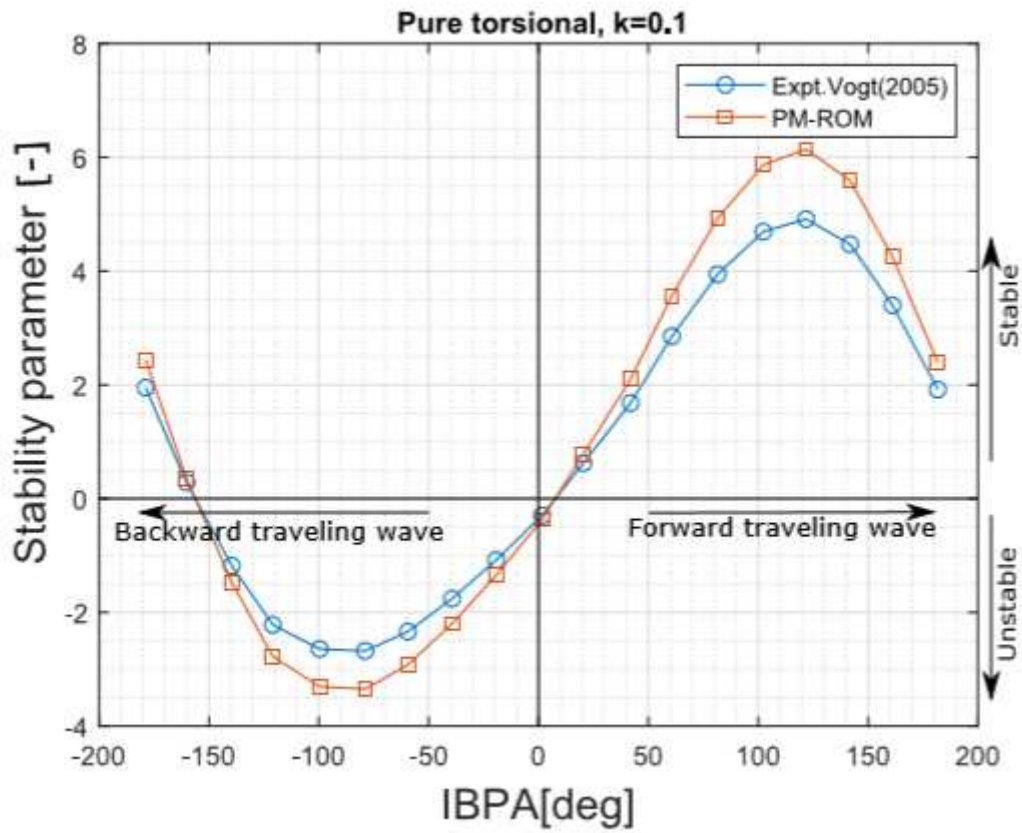


Figure 35

AD vs IBPA s-curve of reference blade for torsional flutter at low subsonic, nominal inflow OP , k=0.1

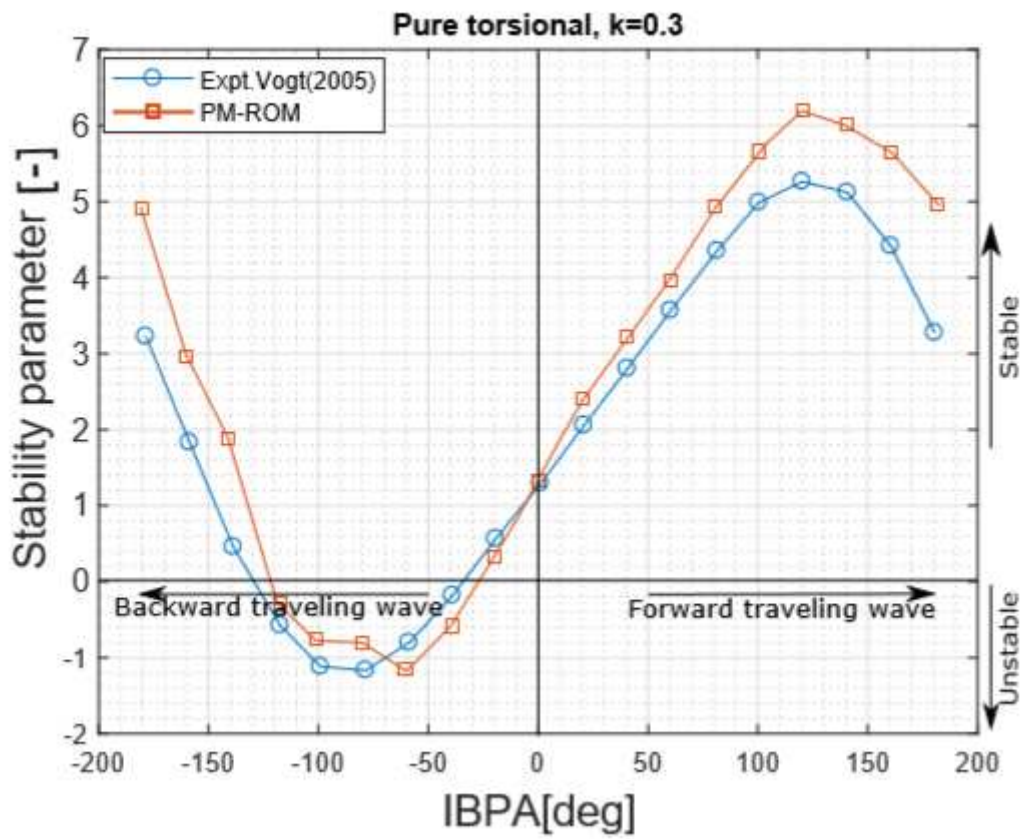


Figure 36

AD vs IBPA curve of reference blade for torsional mode flutter; low subsonic, nominal inflow OP , K=0.3